

Scalable Pixel-based Reconfigurable Beamforming Networks for Designing Fluid Antenna Systems

Jichen Zhang, *Student Member, IEEE*, Junhui Rao, *Member, IEEE*, Tianqu Kang, *Student Member, IEEE*, Zhaoyang Ming, *Student Member, IEEE*, Yijun Chen, *Student Member, IEEE*, Alikhan Umirbayev, *Student Member, IEEE*, Chi-Yuk Chiu, *Senior Member, IEEE*, Ross Murch, *Fellow, IEEE*

Abstract—A novel scalable pixel-based reconfigurable beamforming network (PRBFN) that can be used to form a Fluid Antenna System (FAS), referred to as a PRBFN-FAS, is introduced. The concept of FAS has emerged as an attractive new technology for use in sixth-generation (6G) wireless systems, but most implementations of FAS rely on mechanically reconfigurable antennas which are hindered by inertia, and are therefore too slow to be useful. Using the insight that changing an antenna's physical position is equivalent to switching the excitation current vector of a multi-port antenna, a novel beamformer is proposed with a scalable methodology for incorporating into FAS to form a PRBFN-FAS. Key novelties in creating the PRBFN include selecting the required current vectors and concatenating beamforming networks together to form the desired PRBFN. Two PRBFN-FAS design examples are demonstrated with FAS equivalent physical movements of 0.5 and 1.5 wavelengths. Measurements demonstrate that the PRBFN-FAS provides good matching and Bessel correlation across the desired bandwidth, satisfying FAS requirements. System-level experiments confirm the viability of PRBFN-FAS in practical communication scenarios.

Index Terms—Beamforming, fluid antenna system (FAS), fluid antenna multiple access (FAMA), high switching speed, multiple-input multiple output (MIMO), pattern correlation, pixel-based reconfigurable beamforming network (PRBFN).

I. INTRODUCTION

DRIVEN by the relentless growth in wireless data and the promise of new technology such as Integrated Sensing and Communications (ISAC) and Artificial Intelligence (AI), the research community is now focusing on sixth generation (6G) wireless communication systems. Among the core requirements of 6G networks [1]–[3], ultra-reliable, low-latency, and stable connectivity remain a core target, and cannot be delivered by current wireless techniques. While Multiple-Input Multiple-Output (MIMO) systems can be extended further, these require large antenna arrays and numerous RF chains, introducing significant pressure on signal processing, channel estimation, energy consumption and cost [4].

Manuscript received 15 November 2025; revised 22 December 2025; accepted 28 December 2025. Date of publication 24 January 2026; date of current version 30 June 2026. This work was supported by the Hong Kong Research Grants Council Collaborative Research Fund under Grant AoE/E-601/22-R. (Corresponding author: Junhui Rao.)

Jichen Zhang, Junhui Rao, Tianqu Kang, Zhaoyang Ming, Yijun Chen, Alikhan Umirbayev, and Chi-Yuk Chiu are with the Department of Electronic and Computer Engineering, the Hong Kong University of Science and Technology, Hong Kong (e-mail: jzhangiq@connect.ust.hk, jraoa@connect.ust.hk).

Ross Murch is with the Department of Electronic and Computer Engineering and the Institute for Advanced Study (IAS), the Hong Kong University of Science and Technology, Hong Kong (e-mail: eermurch@ust.hk).

In this context, the concept of the Fluid Antenna System (FAS) has been proposed as a potential enabling technology for 6G [5], [6]. Unlike antennas locked to fixed locations such as in MIMO, the concept of FAS is to sweep a single radiator across a physical space with fine resolution. This change is important because it makes more effective use of the spatial dimension without increasing the number of RF chains compared to MIMO. A typical FAS scheme is depicted in Fig. 1(a), where FAS dynamically selects one of N possible physical positions for the antenna. These antenna positions are referred to as FAS "ports", and in this example there are N FAS ports evenly distributed across the $W\lambda$ linear space (where W is in units of wavelength λ) in a rich scattering environment [5]. In Fig. 1(b), typical received signals for the FAS are shown from two base stations where it can be observed the fading of the received signal from each basestation is largely independent. By exploiting the peaks and nulls of the signal envelope across the FAS ports, significant enhancements to wireless communication system performance have been shown [5], [6]. For example, FAS can maximize Signal-to-Interference Ratio (SIR). It can also facilitate multi-user access without complex signal processing [7], [8], also referred to as fluid antenna multiple access (FAMA) [9].

It is also worth noting that the term "fluid" in FAS is metaphorical [6], [10]: it includes any system where the position and shape of the antenna can be flexible and is selected by the wireless system to optimize a performance metric. FAS does not prescribe that the hardware must literally be made of fluid [10], and any technology that can reconfigure the antenna system is suitable [6], [10].

Extensive system simulations have demonstrated that FAS can significantly enhance communication performance and provide strong support for cutting-edge technologies, such as ISAC [11], [12] and reconfigurable intelligent surfaces (RISs) [13]. However, when the spotlight turns from algorithms to hardware, the literature thins drastically. The few FAS prototypes reported so far split into three kinds. The first category is based on physical-movement-based reconfigurable antennas, including motor-driven movement [14], pump-controlled fluid displacement [15], [16], or electrowetting-based droplets manipulation [17]. The operating principles of these antennas are straightforward. However, their FAS port switching speed is too slow for millisecond-scale wireless channel dynamics, limiting their FAS potential [18]. As a second category, meta-fluid antennas, creating diode-controlled slots across a waveguide as FAS ports, can be an FAS option [19]. With great

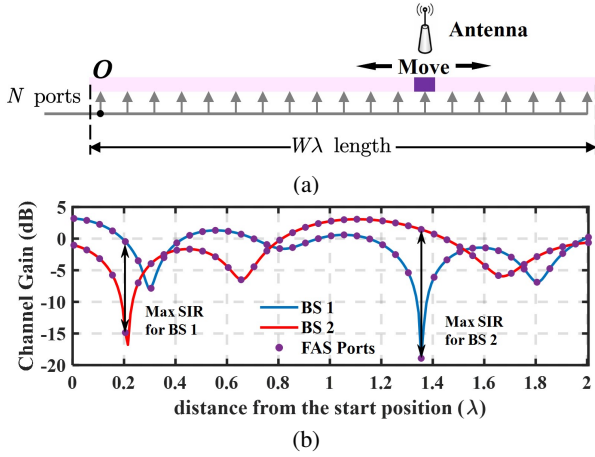


Fig. 1. FAS System. (a) Typical FAS configuration with N ports across a $W\lambda$ linear space operating in a rich scattering environment. (b) Signals received by the FAS from two different base stations, BS 1 (blue line) and BS 2 (red line). The signals are finely sampled across 2λ and since the FAS is in a rich scattering environment the signals from each base station fade independently. Therefore selecting an FAS port position with the largest signal can boost wireless performance (see max SIR points for BS 1 and BS 2) for example.

scalability and compatibility with PCBs, meta-fluid antennas achieve microsecond switching speeds that can timely track fading wireless channels. However, the required $\lambda/2$ slot size inherently limits FAS port density (N/W), resulting in sparse spatial sampling which reduces spatial diversity and ultimately compromises the performance of FAS [5], [9].

In the third category, pixel-based reconfigurable antennas (PRAs) can also implement FAS [20]. The PRA employs sub-wavelength metallic pixels interconnected via RF switches, enabling dynamic control of current distribution and thus radiation patterns. Through optimized design, its reconfigurable states can emulate spatial correlations of FAS, such as the Bessel function, effectively emulating FAS behavior. For instance, the PRA in [20] emulates a FAS with $W = 0.5$ and $N = 12$. With microsecond switching and high port density, PRAs fully release the spatial diversity of FAS, and recent studies have explored their applications in communication systems [21], [22]. However, scalability is limited by the $\lambda/2$ antenna size, which constrains achievable W values, while the nonlinearity of PIN diodes restricts PRAs to low power level cases (< 15 dBm) [23], preventing their deployments at the transmitter (Tx).

To address the challenges above, a fourth category of FAS based on beamforming networks (BFNs) offers a new possibility. By switching the BFN states, the BFN can combine a set of orthogonal radiation patterns that mimic the fine antenna position requirement in FAS, while maintaining μs switching speed. In addition, the BFN can be positioned ahead of power amplifiers (PAs), in order to keep the reconfigurable devices, including PIN diodes or varactors [24]–[27], within their linear operating region. This eliminates nonlinear distortion, and permits Tx-side deployment. Moreover, the BFN is scalable, thus it can achieve large FAS size W , breaking the size limitation of PRA-FAS.

In this paper, a pixel-based reconfigurable beamforming network (PRBFN) is proposed for FAS applications, referred to as PRBFN-FAS. Its design methodology, measurements, and

experiments are described. The key novelties and distinctive features can be summarized as follows.

1) *Novel implementation of FAS using beamforming*: By mapping each available FAS port to predefined excitation currents, port selection in FAS is shown to be equivalent to beamforming. Based on our PRBFN-FAS design, we provide a beamforming-based framework for FAS implementation.

2) *High reconfigurability with high port density*: Our PRBFN-FAS can support numerous (N) states, thereby enabling the high port density required for FAS. Pixel-based reconfigurable structures enable precise control of the required excitation beamforming currents providing the required FAS port correlation [28]–[31].

3) *Scalable cascaded topology with high scalability*: Our design for the PRBFN-FAS adopts a cascaded topology composed of identical unit cells, each with one input and two outputs. FAS with large W is achieved by cascading multiple unit cells. In principle, this cascaded topology is limited only by insertion loss, which can be compensated by additional amplifiers.

4) *Enhanced linearity for transmitter applications*: Previous high-speed FAS designs faced challenges in Tx applications [19], [20] due to the nonlinearity of PIN diodes under high-power operation [23]. The proposed PRBFN-FAS overcomes this by placing the PRBFN before PAs, guaranteeing small-signal conditions of reconfigurable components such as diodes.

5) *Stable pattern correlation relationship*: The proposed PRBFN-FAS provides stable output amplitude and phase combinations across a bandwidth exceeding 5%, ensuring the required port correlation for numerous states and enabling practical applications. While the spatial correlation of N FAS ports naturally follows a Bessel function, keeping the relationship over a wide bandwidth is challenging and the PRBFN-FAS approach overcomes this. In contrast, the PRA FAS design in [20] achieves only a 2% bandwidth, restricting it to principle verification.

6) *Methodology, prototypes and measurements*: This work proposes a comprehensive PRBFN-FAS design methodology suitable for FAS with any size W and port number N . The effectiveness of this methodology is demonstrated through the design, fabrication, and testing of two prototypes with distinct parameters, $W = 0.5, N = 11$ and $W = 1.5, N = 18$, respectively. The good agreement between measured and simulated results confirms the validity of our approach.

The remainder of the paper is organized as follows. Section II is a theoretical analysis, which explains how FAS is realized through beamforming. The PRBFN-FAS architecture is also provided. Section III presents the design methodology of the PRBFN-FAS. In Section IV, two PRBFN-FAS designs with various FAS parameters ($W = 0.5, N = 11$, and $W = 1.5, N = 18$) are described, covering the detailed architecture, fabricated prototypes, and measured results. Section V reports system-level experiments of the PRBFN-FAS, including wireless channels and correlation measured in a real scattering environment. In Section VI, further discussion is provided, and comparison with previous related works. Finally, we summarize and draw conclusions in Section VII.

II. DESIGN ANALYSIS

A. Background: From Spatial to Pattern Correlation

To understand how beamforming can realize FAS, we must first establish that beamforming radiation patterns are functionally equivalent to switching the physical positions of the radiators in conventional FAS. To demonstrate this equivalence, we analyze both systems under rich scattering environments where polarizations are spatially uncorrelated and equally likely [32], and follow the analysis approach described in [20].

For FAS with a size of $W\lambda$ and port number N , we assume that the far-field radiation pattern at the n -th FAS port can be written as $\mathbf{e}_n(\boldsymbol{\Omega}) = [e_{\theta,n}(\boldsymbol{\Omega}), e_{\phi,n}(\boldsymbol{\Omega})]^T$, where $\boldsymbol{\Omega} = (\theta, \phi)$. All N radiation patterns share a common coordinate origin O and the voltage at the n -th port is denoted as

$$g_n = a \iint \mathbf{e}_n(\boldsymbol{\Omega}) \cdot \mathbf{h}(\boldsymbol{\Omega}) d\boldsymbol{\Omega}, \quad (1)$$

where a is a proportionality constant [33], and $\mathbf{h}(\boldsymbol{\Omega}) = [h_\theta(\boldsymbol{\Omega}), h_\phi(\boldsymbol{\Omega})]^T$ represents the incidence field from the scattering environments.

The correlation coefficient of the i -th and j -th FAS port, $C_{i,j}$, is computed by

$$C_{i,j} = \frac{\mathcal{E}[g_i g_j^*]}{\sqrt{\mathcal{E}[|g_i|^2] \mathcal{E}[|g_j|^2]}} = \frac{\text{Cov}(g_i, g_j)}{\sqrt{\mathcal{E}[|g_i|^2] \mathcal{E}[|g_j|^2]}}, \quad (2)$$

where $\mathcal{E}[\cdot]$ presents the expectation, and $g_n \sim \mathcal{CN}(0, \sigma_n^2)$ is attributed to the randomness of scatterings. Using (1) the numerator of (2) can be expanded as

$$\text{Cov}(g_i, g_j) = a^2 \mathcal{E} \left[\iint \mathbf{e}_i(\boldsymbol{\Omega}) \cdot \mathbf{e}_j^*(\boldsymbol{\Omega}) \cdot S(\boldsymbol{\Omega}) d\boldsymbol{\Omega} \right], \quad (3)$$

where $S(\boldsymbol{\Omega}) = \mathcal{E}[\mathbf{h}(\boldsymbol{\Omega}) \cdot \mathbf{h}^*(\boldsymbol{\Omega})]$ is the power angular spectrum (PAS) over 3D space. Therefore the correlation coefficient $C_{i,j}$ can be expressed in terms of radiation patterns, as

$$C_{i,j} = \frac{\iint \mathbf{e}_i \cdot \mathbf{e}_j^* \cdot S d\boldsymbol{\Omega}}{\sqrt{\iint |\mathbf{e}_i|^2 \cdot S d\boldsymbol{\Omega}} \sqrt{\iint |\mathbf{e}_j|^2 \cdot S d\boldsymbol{\Omega}}}, \quad (4)$$

where $\boldsymbol{\Omega}$ is omitted for brevity, and $S(\boldsymbol{\Omega}) = S_0 \mathbf{U}_2$ in which \mathbf{U}_2 is the 2×2 identity matrix due to the polarization components over 3D space [32] being independent in a rich scattering environment.

For conventional FAS in Fig. 1, switching the location of the activated port alters the radiation pattern. Specifically, all N ports share identical amplitude patterns with $|\mathbf{e}_i(\boldsymbol{\Omega})| = |\mathbf{e}_j(\boldsymbol{\Omega})|$, while their phases can be related by

$$\mathbf{e}_j(\boldsymbol{\Omega}) = \mathbf{e}_i(\boldsymbol{\Omega}) \cdot e^{jk d_{i,j} \cos \phi \sin \theta}, \quad (5)$$

where $d_{i,j} = \frac{|i-j|W\lambda}{N-1}$ is the distance between the i -th and j -th FAS ports. Using (2) to (5) and considering PAS with isotropic patterns in the $x-y$ plane only, the correlation $C_{i,j}$ (also the spatial correlation) becomes

$$C_{i,j} = \iint e^{-jk d_{i,j} \cos \phi \sin \theta} \delta(\theta - \frac{\pi}{2}) d\boldsymbol{\Omega} = J_0 \left(\frac{2\pi|i-j|W}{N-1} \right), \quad (6)$$

where $S(\boldsymbol{\Omega}) = \delta(\theta - \frac{\pi}{2})$ [32], and $J_0(\cdot)$ is the Bessel function of the first kind, order zero [34], agreeing with the proposed model in [5].

It should also be observed that the phase of the correlation coefficient $C_{i,j}$ is not critical for evaluating FAS performance, since key metrics, such as channel capacity [5] and multiplexing gain [9], solely depend on the magnitudes of FAS port voltages. Therefore, the absolute value is introduced in (4), as

$$C_{i,j} = \left| \frac{\iint \mathbf{e}_i \cdot \mathbf{e}_j^* \cdot S d\boldsymbol{\Omega}}{\sqrt{\iint |\mathbf{e}_i|^2 \cdot S d\boldsymbol{\Omega}} \sqrt{\iint |\mathbf{e}_j|^2 \cdot S d\boldsymbol{\Omega}}} \right|, \quad (7)$$

and similarly for conventional FAS (6) becomes

$$C_{i,j} = \left| J_0 \left(\frac{2\pi|i-j|W}{N-1} \right) \right|, \quad (8)$$

which serves as the final target expression for FAS correlation.

Comparing equations (7) and (8), it can be observed that carefully selecting patterns that satisfy the specific spatial correlation requirements in (8), can also emulate spatially distributed FAS ports [20]. This approach effectively converts spatial correlation between FAS ports into pattern correlation between patterns and was the approach taken in the PRA design for an FAS reported in [20]. It also suggests that other approaches to obtaining the desired patterns for FAS can also be utilized, and conventional beamforming is one such alternative approach. Therefore, in this paper, we are proposing to utilize beamforming, instead of PRAs, for obtaining the required patterns for FAS. In particular, we are proposing finding appropriate excitation currents to feed fixed position antennas that can provide the required FAS patterns. As a result, the key is obtaining the beamforming excitation currents which in this work is performed with novel PRBFN structures.

In the remainder of this work, the development is for FAS transmitter configurations. We select this configuration because the pixel-based approach to FAS [20] suffers from non-linearity when the transmit power is more than 15 dBm [23] due to the use of active components, while our novel PRBFN avoids that issue. The PRBFN approach can also be configured as a receiver (Rx) straightforwardly and that is described at the end of the paper.

B. Spatial Correlation using Beamforming

The proposed beamforming architecture for FAS is illustrated in Fig. 2. The single RF chain of the FAS feeds the input of the PRBFN, whose outputs are connected to a multiport antenna with N_A antenna ports via N_A PAs. The PRBFN can generate N reconfigurable beamformer states, corresponding to N FAS ports. The PAs are inserted after the PRBFN so that the PRBFN can operate at lower power levels, thus avoiding linearity issues.

The radiation pattern matrix of the multiport antenna can be defined as $\mathbf{E}_M = [\mathbf{e}_1^M, \mathbf{e}_2^M, \dots, \mathbf{e}_{N_A}^M]$, where $\boldsymbol{\Omega}$ is omitted for simplicity, and $\mathbf{e}_m^M(\boldsymbol{\Omega})$, $m = 1, 2, \dots, N_A$ is the radiation pattern of the m -th antenna port excited by unit current with all other ports matched.

The implementation of FAS through beamforming necessitates N reconfigurable beamforming patterns. This means

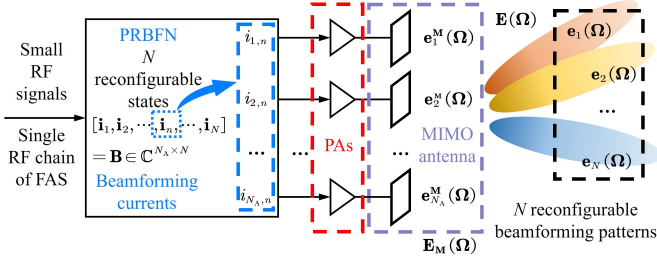


Fig. 2. Architecture of the proposed PRBFN-FAS, including the PRBFN with N reconfigurable states, and a multiport antenna with N_A feeding ports that are all well isolated. N desired reconfigurable radiation patterns that follows the Bessel correlation (6) for FAS, can be realized.

that the PRBFN must support N distinct reconfigurable states, aligning with the number of FAS ports. The output excitation current vector of the n -th PRBFN state can be written as $\mathbf{i}_n = [i_{1,n}, i_{2,n}, \dots, i_{N_A,n}]^T \in \mathbb{C}^{N_A \times 1}$. Therefore, the n -th reconfigurable beamforming radiation pattern $\mathbf{e}_n(\Omega)$ is

$$\mathbf{e}_n(\Omega) = \sum_{m=1}^{N_A} \mathbf{e}_m^M(\Omega) i_{m,n} = \mathbf{E}_M \mathbf{i}_n. \quad (9)$$

The excitation current vectors of all N states can be collected into a beamforming current matrix \mathbf{B} , expressed as

$$\mathbf{B} = [\mathbf{i}_1, \mathbf{i}_2, \dots, \mathbf{i}_N] \in \mathbb{C}^{N_A \times N}. \quad (10)$$

Thus N reconfigurable beamforming radiation patterns fed by N PRBFN states, written as $\mathbf{E}(\Omega)$, are given by

$$\mathbf{E} = [\mathbf{e}_1, \mathbf{e}_2, \dots, \mathbf{e}_N] = \mathbf{E}_M \mathbf{B}, \quad (11)$$

where we omit (Ω) for brevity.

The correlation relationship between the N beamforming radiation patterns can be found as [35]

$$\begin{aligned} \mathbf{C} &= \left| \iint \mathbf{E}^H \mathbf{E} S d\Omega \right| = \left| \iint \mathbf{B}^H \mathbf{E}_M^H \mathbf{E}_M \mathbf{B} S d\Omega \right| \\ &= \left| \mathbf{B}^H \left(\iint \mathbf{E}_M^H \mathbf{E}_M S d\Omega \right) \mathbf{B} \right| = |\mathbf{B}^H \mathbf{K}_M \mathbf{B}|, \end{aligned} \quad (12)$$

where the denominator for normalization, as presented in (7), is omitted for brevity. Notably, $\mathbf{K}_M \in \mathbb{C}^{N_A \times N_A}$, the pattern correlation of the MIMO antenna, is determined exclusively by the N_A patterns of the multiport antenna, independent of the PRBFN. Given sufficiently high isolation between the antenna ports, \mathbf{K}_M can be approximated as an identity matrix \mathbf{U}_{N_A} . Consequently, the correlation relationship $\mathbf{C} \in \mathbb{C}^{N \times N}$ in (12) of the N PRBFN-FAS radiation patterns can be simplified to

$$\mathbf{C} = |\mathbf{B}^H \mathbf{B}|. \quad (13)$$

When all antenna ports are well-matched to a standard characterized impedance Z_0 , the N excitation current vectors collected in \mathbf{B} are determined exclusively by the PRBFN. This characteristic decouples the PRBFN design process from the subsequent design of the multiport antenna, allowing these two parts to be developed independently.

The multiport antenna with N_A ports must exhibit excellent port matching and low mutual coupling to ensure that \mathbf{K}_M approximates an identity matrix. Meanwhile, the PRBFN must

be carefully designed to generate N reconfigurable states that produce a specific excitation current matrix \mathbf{B} , resulting in a correlation matrix \mathbf{C} that satisfies the desired Bessel correlation matrix (8).

In the next Section, we will discuss the design methodology of the PRBFN.

III. PRBFN DESIGN METHODOLOGY

The design methodology for the PRBFN includes four key steps. First, the FAS parameters, W , N , and the target correlation are specified. Second, based on these parameters, the \mathbf{B} used to generate N beamforming excitation currents is optimized so that it approximates the desired correlation, yielding an optimal solution that guides the subsequent PRBFN configuration. Third, a PRBFN topology, consisting of cascaded unit cells, is found based on the results above. Finally, the structure of the unit cells are found and designed.

A. Select FAS Parameters

As a method to realize FAS, the proposed PRBFN-FAS adopts standard FAS parameters, including the number of FAS ports N , the size $W\lambda$ and target correction. To realize its full potential, appropriate parameter selection is essential and we rely on previous work to select these. The target correlation is denoted as \mathbf{C}_{obj} [34], and the (i, j) -th entry of \mathbf{C}_{obj} is defined by (8), as

$$[\mathbf{C}_{\text{obj}}]_{i,j} = \left| J_0 \left(\frac{2\pi|i-j|W}{N-1} \right) \right|. \quad (14)$$

Another key parameter is the FAS port density, denoted as N/W . Using previous results in [5], [9], the rate of increase in channel capacity and multiplexing gain significantly decreases as the FAS port density satisfies $N/W \geq 10$. Considering the increasing design complexity with higher port density, we maintain $N/W = 10$ as a sufficient condition in the following PRBFN-FAS designs.

B. Find Optimal $\hat{\mathbf{B}}$

For a given W (e.g. $W = 0.5$ and $W = 1.5$ in the two examples in our work) we select $N = 10W$ to satisfy our FAS port density requirement. Substituting \mathbf{C}_{obj} into equation (13), a closed-form solution for $\mathbf{B} \in \mathbb{C}^{N_A \times N}$ exists via singular value decomposition (SVD) when $N = N_A$. But N will typically be much larger than N_A (to provide the necessary correlation), and therefore a minimum least squares formulation using SVD should be used. However, we are not concerned about the phase of the correlation matrix (13) in FAS, and therefore our target is on the correlation of $|\mathbf{B}^H \mathbf{B}|$. This leads to a greater possibility for finding excellent solutions, but it also leads to non-uniqueness, implying there are multiple feasible solutions among which we find the optimum. Thus, we adopt a numerical optimization approach to find an optimal beamforming current matrix \mathbf{B} , denoted as $\hat{\mathbf{B}}$, such that the resulting correlation approximates \mathbf{C}_{obj} as closely as possible.

To minimize the deviation between the target correlation matrices, we formulate the following optimization problem for a system with N_A antenna ports

$$\begin{aligned} \min_{\mathbf{B}} f_{N_A}(\mathbf{B}) &= \|\mathbf{B}^H \mathbf{B} - \mathbf{C}_{\text{obj}}\|_F^2 \\ \text{s.t. } \|\mathbf{i}_n\|_2^2 &= 1, \quad \forall n = 1, 2, \dots, N, \end{aligned} \quad (15)$$

where $\|\cdot\|_F$ denotes the Frobenius norm, and \mathbf{i}_n is the n -th vector of \mathbf{B} in (10), following the energy constraint. The optimal solution of (15) is the desired PRBFN output

$$\hat{\mathbf{B}} = [\hat{\mathbf{i}}_1, \hat{\mathbf{i}}_2, \dots, \hat{\mathbf{i}}_N] \quad (16)$$

where $\hat{\mathbf{i}}_n = [\hat{i}_{1,n}, \hat{i}_{2,n}, \dots, \hat{i}_{N_A,n}]^T \in \mathbb{C}^{N_A \times 1}$. Since \mathbf{B} has dimensions $\mathbb{C}^{N_A \times N}$, the error $f_{N_A}(\mathbf{B})$ is also a function of N_A as is indicated by the subscript.

Given that the optimization variables \mathbf{B} belong to the complex domain, and the objective function contains absolute values, solving this optimization problem presents significant challenges. To address this, we employ the projected gradient descent (PGD) method and incorporate modifications based on $\mathbb{C}\mathbb{R}$ -calculus [36], enabling effective application to this complex optimization problem.

To apply the PGD method, we first derive the gradient of the objective function $f_{N_A}(\mathbf{B})$ with respect to the complex matrix \mathbf{B} . The objective function in (15) can be expanded as

$$f_{N_A}(\mathbf{B}) = \sum_{i=1}^N \sum_{j=1}^N (|\mathbf{B}^H \mathbf{B}|_{i,j} - [\mathbf{C}_{\text{obj}}]_{i,j})^2, \quad (17)$$

where $[\mathbf{B}^H \mathbf{B}]_{i,j}$ denotes the (i,j) -th element of the product. Since \mathbf{B} is complex, we use Wirtinger calculus [37], treating \mathbf{B} and its conjugate \mathbf{B}^H as independent variables. This gradient with respect to \mathbf{B} is given by

$$\nabla_{\mathbf{B}} f_{N_A} = 2\mathbf{B} \left[(|\mathbf{B}^H \mathbf{B}| - \mathbf{C}_{\text{obj}}) \circ \frac{\mathbf{B}^H \mathbf{B}}{|\mathbf{B}^H \mathbf{B}|} \right], \quad (18)$$

where \circ denotes the Hadamard product, and the $\frac{\mathbf{B}^H \mathbf{B}}{|\mathbf{B}^H \mathbf{B}|}$ calculation is the element-wise computation. Applying the sign function to $\mathbf{B}^H \mathbf{B}$ as

$$\text{sgn}(\mathbf{B}^H \mathbf{B}) = \frac{(\mathbf{B}^H \mathbf{B})^H}{|\mathbf{B}^H \mathbf{B}|}, \quad (19)$$

where the operations inside the brackets are performed element-wise. Thus the gradient can be succinctly written as

$$\nabla_{\mathbf{B}} f_{N_A} = 2\mathbf{B} [(|\mathbf{B}^H \mathbf{B}| - \mathbf{C}_{\text{obj}}) \circ \text{sgn}(\mathbf{B}^H \mathbf{B})]. \quad (20)$$

Given the constraint that each column of \mathbf{B} must have unit norm, the PGD method is utilized. This involves iteratively performing gradient descent steps followed by projection onto the feasible set defined by the constraints. The pseudo code for iterative PGD is given in Algorithm 1.

For a set of given W and N , Algorithm 1 can be applied to find the optimum $\hat{\mathbf{B}}$ with different values of N_A . To determine a suitable but minimal N_A , the relative error $\epsilon(N_A)$ is denoted by

$$\epsilon(N_A) = \frac{f_{N_A}(\hat{\mathbf{B}})}{f_{N_A}(\hat{\mathbf{B}}')} = \frac{\|\hat{\mathbf{B}}^H \hat{\mathbf{B}} - \mathbf{C}_{\text{obj}}\|_F^2}{\|(\hat{\mathbf{B}}')^H \hat{\mathbf{B}}' - \mathbf{C}_{\text{obj}}\|_F^2}, \quad (21)$$

Algorithm 1 PGD Optimization for $\hat{\mathbf{B}}$

Input: Target Bessel correlation: $\mathbf{C}_{\text{obj}} \in \mathbb{R}^{N \times N}$,

Antenna ports N_A , step size $\eta > 0$, tolerance $\varepsilon > 0$,

$\mathbf{B}^{(0)} = [\mathbf{i}_1^{(0)}, \mathbf{i}_2^{(0)}, \dots, \mathbf{i}_N^{(0)}] \in \mathbb{C}^{N_A \times N}$,

$\Rightarrow \|\mathbf{i}_n^{(0)}\|_2^2 = 1, \quad \forall n = 1, 2, \dots, N$.

```

1: for  $k = 1$  to maxIter do
2:   Gradient computation: Compute the gradient  $\nabla_{\mathbf{B}} f_{N_A}$ 
     of current iterate  $\mathbf{B}^{(k-1)}$  by (20).
3:   Gradient descent step: Update  $\mathbf{B}^{(k-1)}$  with  $\mathbf{B}^{(k)}$  by
     moving to the negative gradient direction.
4:      $\mathbf{B}^{(k)} = \mathbf{B}^{(k-1)} - \eta \cdot \nabla_{\mathbf{B}} f_{N_A}$ 
5:   Projection: Project  $\mathbf{B}^{(k)}$  onto the set of matrices where
     each column follows unit norm.  $\Rightarrow$  constraint in (15).
6:   for  $n = 1, 2, \dots, N$  do
7:      $i_{\text{norm}}^2 = \|\mathbf{i}_n^{(k)}\|_2^2$ 
8:     if  $i_{\text{norm}}^2 \neq 0$  then
9:       Normalization:  $\mathbf{i}_n^{(k)} = \mathbf{i}_n^{(k)} / i_{\text{norm}}$ 
10:    else
11:      Initialize  $\mathbf{i}_n^{(k)}$  as a random unit vector.
12:    end if
13:  end for
14:  Convergence check: Compute the objective function
     through (15):  $f_{N_A}(\mathbf{B}^{(k)}) = \|\mathbf{B}^{(k)H} \mathbf{B}^{(k)} - \mathbf{C}_{\text{obj}}\|_F^2$ 
15:  if  $f_{N_A}(\mathbf{B}^{(k)}) < \varepsilon$  then
16:    Output  $\hat{\mathbf{B}} = \mathbf{B}^{(k)}$  and terminate.
17:  end if
18: end for
Output:  $\hat{\mathbf{B}} \in \mathbb{C}^{N_A \times N}$ , make  $\hat{\mathbf{C}} = |\hat{\mathbf{B}}^H \hat{\mathbf{B}}| \approx \mathbf{C}_{\text{obj}}$ .

```

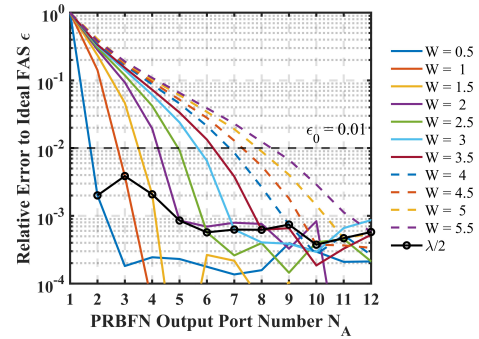


Fig. 3. In PRBFN-FAS, the relative error ϵ of optimized correlation result $|\hat{\mathbf{B}}^H \hat{\mathbf{B}}|$ against target Bessel \mathbf{C}_{obj} versus PRBFN output port number N_A , with the FAS port density of $N/W = 10$.

where the denominator for normalization is the error f_{N_A} achieved by setting $N_A = 1$. In this configuration, $|(\hat{\mathbf{B}}')^H \hat{\mathbf{B}}'| \in \mathbb{C}^{N \times N}$ is the all-one matrix since there is only one antenna.

Assuming FAS port density as $N/W = 10$, the $\epsilon(N_A)$ with various W are plotted in Fig. 3. The results indicate that the error between the optimal correlation $|\hat{\mathbf{B}}^H \hat{\mathbf{B}}|$ and the ideal FAS correlation \mathbf{C}_{obj} decreases monotonically with increasing N_A . When the error falls below a certain threshold, such as less than 10^{-3} , the curves flatten due to numerical errors. We set a threshold $\epsilon_0 = 0.01$ and select the smallest N_A that satisfies $\epsilon(N_A) < \epsilon_0$.

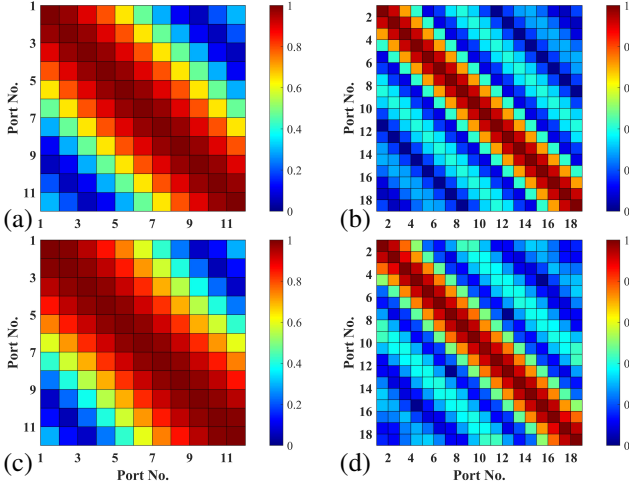


Fig. 4. Ideal Bessel correlation matrix \mathbf{C}_{obj} with (a) $W = 0.5, N = 11$ and (b) $W = 1.5, N = 18$. Corresponding optimized correlation $[\mathbf{B}^H \mathbf{B}]$ with (c) $N_A = 2$ and (d) $N_A = 4$. Relative errors are (c) $\epsilon(N_A) = 0.008$ and (d) $\epsilon(N_A) = 0.001$, respectively.

We can see from Fig. 3 that the required N_A is directly related to W . A simple but effective approach to finding an approximate relation is to consider the standard $\lambda/2$ separation for antennas in MIMO systems, where N_A satisfies

$$N_A \geq \lfloor W/0.5 \rfloor + 1, \quad (22)$$

in which $\lfloor \cdot \rfloor$ denotes the floor function. In Fig. 3, using this minimal N_A , it can be observed that $\epsilon(N_A)$ falls below ϵ_0 with various W , ensuring that \mathbf{C}_{obj} is approached as closely as possible. That is, the number of antennas N_A required in our beamforming FAS can be determined by (22).

To validate the effectiveness of the proposed optimization method, we present two design examples with parameters $W = 0.5, N = 11, N_A = 2$ and $W = 1.5, N = 18, N_A = 4$. Their ideal Bessel correlation matrices \mathbf{C}_{obj} are shown in Fig. 4(a) and (b), respectively. The optimal correlation results $\hat{\mathbf{C}} = [\mathbf{B}^H \hat{\mathbf{B}}]$ obtained through our optimization approach are depicted in Fig. 4(c) and (d). Comparing with the ideal results in Fig. 4(a) and (b), it can be observed that the optimized correlation matrices closely match the ideal ones, demonstrating the effectiveness of the proposed PGD optimization.

Furthermore, during the optimization process, multiple beamforming currents $\hat{\mathbf{B}}$ satisfying the performance criteria can be obtained. Given that the PGD in Algorithm 1 is an efficient linear optimization process, we randomly generate 30 initial $\mathbf{B}^{(0)}$ using a uniform distribution with unit constraint for each column, and run Algorithm 1 for each $\mathbf{B}^{(0)}$ to obtain 30 optimal $\hat{\mathbf{B}}$. Among all available results, we select the $\hat{\mathbf{B}}$ with the smallest phase differences across N_A output ports. This strategy helps minimize the circuit complexity and physical size of the PRBFN in subsequent implementations, thereby reducing overall design difficulty.

C. Cascaded Topology of the PRBFN

In this subsection, we describe the third step in our design process which uses a cascaded topology for constructing the PRBFN. Given that the FAS employs only a single RF chain

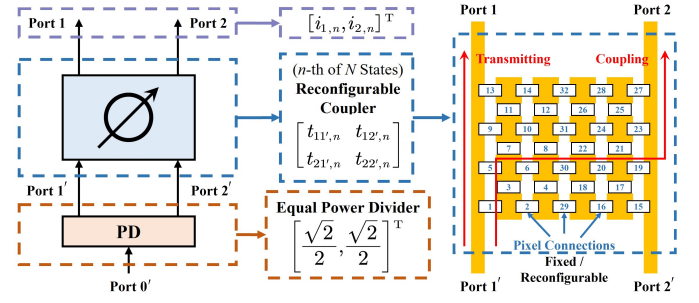


Fig. 5. Unit cell of the PRBFN: a single reconfigurable module that is cascaded to build the full PRBFN. As an example, the pixel-based reconfigurable structure can be integrated inside the coupler.

but requires N_A outputs, we introduce a unit cell with one input port and two output ports, as illustrated in Fig. 5. This unit cell can then be cascaded to form N_A output ports, as shown in Fig. 6. Each unit is composed of a 3 dB equal power divider (PD) followed by a four-port reconfigurable coupler. A pixel-based structure is utilized in the coupler to provide reconfiguration, allowing control over both the amplitude and phase of the output currents by adjusting the internal connections between metal pixels [29], [30], [38]. The pixel approach can provide N states for the coupler, providing N sets of N_A output currents for the required FAS design. For each unit cell, we initially assume no losses for methodological simplicity. In later discussions, insertion loss is constrained to avoid excessive signal attenuation in any individual unit.

For clarity, the unit in Fig. 5 corresponds to that highlighted in the red box in Fig. 6. This cell can be identified by its stage (M -th stage) and its vertical position within that stage (which is the 1st in this example), and we therefore denote the currents at its output for the n -th state as $\mathbf{i}_{M,n}^1 = [i_{1,n}^1, i_{2,n}^1]^T$. In addition, for the topology in Fig. 6, the number of PRBFN output ports N_A must be a power-of-two and thus we select $N_A = 2^M$ while following formula in (22). Therefore, for the m -th ($m \leq M$) stage, there are a total of 2^m unit cells.

For the unit cell at the M -th stage, first position (cell in red box in Fig. 6), its output current for the n -th reconfigurable state is given by

$$\mathbf{i}_{M,n}^1 = \mathbf{T}_n \mathbf{p} = \begin{bmatrix} t_{11',n} & t_{12',n} \\ t_{21',n} & t_{22',n} \end{bmatrix} \mathbf{p} \quad (23)$$

where $\mathbf{p} = \frac{\sqrt{2}}{2} [1, 1]^T$ is the PD output vector, $\|\mathbf{i}_{M,n}^1\|_2^2 = 1$ since the input current is normalized to unity and the transmission matrix \mathbf{T}_n of the n -th coupler state satisfies the normalization condition

$$\|\mathbf{T}_n\|_F = \sqrt{\sum_{i=1,2} \sum_{j=1',2'} |t_{ij,n}|^2} = \sqrt{2}. \quad (24)$$

Following equation (23), the output current vector of the k -th ($k \leq 2^{(m-1)}$) cell in the m -th stage can be denoted as $\mathbf{i}_{m,n}^k \in \mathbb{C}^{2 \times 1}$ corresponding to its n -th reconfigurable state. Under good matching conditions, the output currents of the n -th state can be written as

$$\mathbf{i}_n = \mathbf{H}_{M,n} \mathbf{H}_{M-1,n} \cdots \mathbf{H}_{2,n} \mathbf{H}_{1,n}, \quad (25)$$

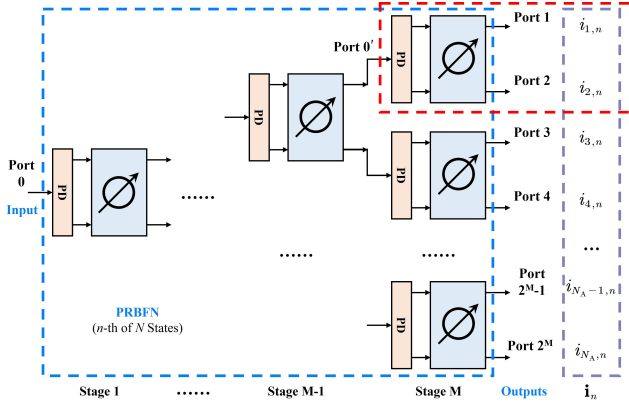


Fig. 6. The M -stage cascaded topology of the proposed PRBFN, with single input (single RF chain of FAS) and $N_A = 2^M$ output ports. The n -th reconfigurable state \mathbf{i}_n of \mathbf{B} is presented.

where $\mathbf{i}_n = [i_{1,n}, i_{2,n}, \dots, i_{N_A,n}]^T \in \mathbb{C}^{2^M \times 1}$, and $\mathbf{H}_{m,n} = \text{blkdiag}(\mathbf{i}_{m,n}^1, \mathbf{i}_{m,n}^2, \dots, \mathbf{i}_{m,n}^{2^{(m-1)}}) \in \mathbb{C}^{2^m \times 2^{(m-1)}}$ is the transmission response of the overall m -th PRBFN stage. To construct the overall architecture of the PRBFN, the complete output beamforming currents \mathbf{B} for all N states must be obtained. This requires solving for all $\mathbf{H}_{m,n}$ in equation (25).

Based on the optimal $\hat{\mathbf{B}}$ gained by the optimization algorithm described previously, the structure of each reconfigurable unit cell within the PRBFN topology, such as the pixel-based configuration illustrated in Fig. 5, can be designed. We aim to optimize each individual module such that the overall output currents \mathbf{B} of the PRBFN in (10) closely approximates the optimal $\hat{\mathbf{B}}$ in (16) across all N reconfigurable states. The PRBFN design follows a backward iterative procedure, starting with the unit modules at the final (M -th) stage and progressing stage-by-stage until reaching the first stage. Following the lossless and matching assumption, the PRBFN design procedure consists of iterative calculations.

The general design process for the PRBFN can be summarized as follows:

1) *Design $2^{(M-1)}$ unit cells for the M -th PRBFN stage:*

According to $\hat{\mathbf{i}}_n \forall n = 1, 2, \dots, N$, we design each unit cell of the M -th stage in PRBFN separately. To illustrate the design process, the unit cell highlighted in the red box in Fig. 6 is taken as an example. In the n -th of N reconfigurable states, the unit cell should satisfy the following conditions

$$\begin{aligned} |i_{1,n}| &= \frac{|\hat{i}_{1,n}|}{\|\hat{\mathbf{i}}_{M,n}^1\|_2}, \quad |i_{2,n}| = \frac{|\hat{i}_{2,n}|}{\|\hat{\mathbf{i}}_{M,n}^1\|_2}, \\ \angle i_{1,n} - \angle i_{2,n} &= \angle \hat{i}_{1,n} - \angle \hat{i}_{2,n}, \end{aligned} \quad (26)$$

where $\hat{\mathbf{i}}_{M,n}^1 = [\hat{i}_{1,n}, \hat{i}_{2,n}]^T$ are the first two terms in the optimal current vector $\hat{\mathbf{i}}_n$ (see (16)). Similarly, the same constraints apply uniformly to all the other units within the M -th PRBFN stage, thus the transmission matrix $\mathbf{H}_{M,n} = \text{blkdiag}(\mathbf{i}_{M,n}^1, \mathbf{i}_{M,n}^2, \dots, \mathbf{i}_{M,n}^{2^{(M-1)}})$ of the M -th PRBFN stage can be derived.

2) *Iterative calculations to obtain the PRBFN:* With the known $\mathbf{H}_{M,n}$ derived above, the conjugate transpose of $\mathbf{H}_{M,n}$

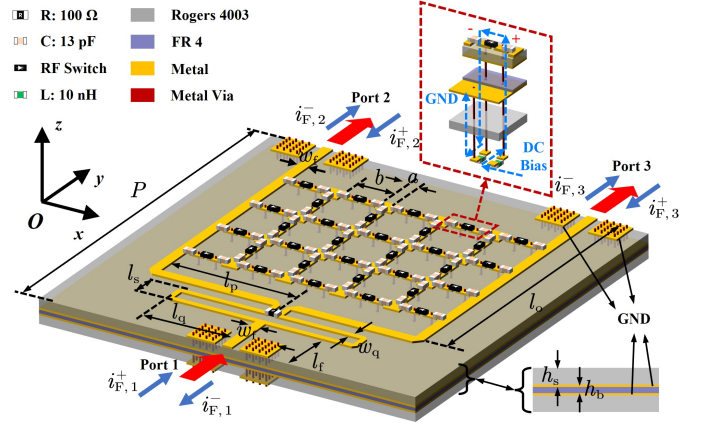


Fig. 7. The configuration of the proposed pixel-based reconfigurable unit cell in the PRBFN topology. Dimensions: $P = 42$, $h_s = 0.508$, $h_b = 0.1$, $w_f = 1.1$, $w_q = 0.6$, $l_f = 6$, $l_s = 2.5$, $l_q = 10$, $l_p = 13.6$, $l_o = 31$, $a = 1.8$, $b = 4$ (Unit: mm).

is taken on both sides of equation (25), yielding

$$\mathbf{H}_{M,n}^H \mathbf{i}_n = (\mathbf{H}_{M,n}^H \mathbf{H}_{M,n}) \mathbf{H}_{M-1,n} \cdots \mathbf{H}_{2,n} \mathbf{H}_{1,n} \quad (27)$$

where the Gram term $(\mathbf{H}_{M,n}^H \mathbf{H}_{M,n})$ can be expanded as

$$\begin{bmatrix} \|\mathbf{i}_{M,n}^1\|_2^2 & 0 & \cdots & 0 \\ 0 & \|\mathbf{i}_{M,n}^2\|_2^2 & \cdots & 0 \\ \vdots & \vdots & \ddots & \vdots \\ 0 & 0 & \cdots & \|\mathbf{i}_{M,n}^{2^{(M-1)}}\|_2^2 \end{bmatrix} = \mathbf{U}_{2^{(M-1)}}, \quad (28)$$

where $\mathbf{U}_{2^{(M-1)}} \in \mathbb{R}^{2^{(M-1)} \times 2^{(M-1)}}$ is the identity matrix. Therefore, (27) can be updated by

$$\mathbf{i}'_n = \mathbf{H}_{M-1,n} \cdots \mathbf{H}_{2,n} \mathbf{H}_{1,n}, \quad (29)$$

where $\mathbf{i}'_n = \mathbf{H}_{M,n}^H \mathbf{i}_n$. The problem thus reduces to the same form as equation (25). Using the same approach as in the previous step, all unit cells of the $(M-1)$ -th stage can be solved. Similarly, the entire PRBFN can be systematically synthesized through this iterative backward solution.

D. Design of Pixel-Based Unit Cell

In the fourth and final step, we find the unit cell design. The structure of the unit cell in our proposed PRBFN is illustrated in Fig. 7, consisting of an equal power divider and a reconfigurable coupler based on a pixel structure. The unit is fabricated using two PCB layers bonded with an intermediate FR4 dielectric substrate. The top PCB layer regulates the amplitude and phase of the RF signal by altering pixel connections via RF switches, enabling multiple reconfigurable states. The bottom PCB layer hosts the control circuit for these RF switches. A detailed view of a single RF switch control structure is provided in the red box of Fig. 7. To ensure signal integrity, the bottom layer employs inductors [39] to isolate RF from the control DC signals, while the upper layer uses capacitors [40] to block DC signals from the RF pathways, thereby facilitating independent control of all independent RF switches by MCUs or FPGAs.

Based on the given circuit architecture, we optimize the pixel internal connections such that the resulting N reconfigurable PRBFN output currents \mathbf{B} for beamforming closely approximates the desired $\hat{\mathbf{B}}$ derived in Section III, satisfying the FAS specifications. Similarly, the unit cell can be modeled as a multi-port network, including 3 external feeding ports and $Q = 32$ internal pixel ports, whose numbers are depicted in Fig. 8(a). We assume that all internal ports are terminated with RF switches serving as loads, specifically, diodes SMP1345-079LF in this design. Corresponding equivalent circuit models of the on and off states are given in Fig. 8(b). The state of each diode can be expressed using a binary vector $\mathbf{x} \in \{0, 1\}^Q$, with "0" and "1" representing off and on state, respectively. The corresponding diagonal load impedance matrix is written as $\mathbf{Z}^L = \text{diag}(Z_1^L, Z_2^L, \dots, Z_Q^L)$.

The voltages and currents of all ports can be related by

$$\begin{bmatrix} \mathbf{v}_F \\ \mathbf{v}_I \end{bmatrix} = \mathbf{Z} \begin{bmatrix} \mathbf{i}_F \\ \mathbf{i}_I \end{bmatrix} = \begin{bmatrix} \mathbf{Z}_{FF} & \mathbf{Z}_{FI} \\ \mathbf{Z}_{IF} & \mathbf{Z}_{II} \end{bmatrix} \begin{bmatrix} \mathbf{i}_F \\ \mathbf{i}_I \end{bmatrix}, \quad (30)$$

where $\mathbf{Z}_{FF} \in \mathbb{C}^{3 \times 3}$ is the impedance matrix between external feeding ports, $\mathbf{Z}_{IF} \in \mathbb{C}^{Q \times 3}$ is the mutual impedance between the source feeding ports and each pixel port, \mathbf{Z}_{FI} is the transpose of \mathbf{Z}_{IF} , and $\mathbf{Z}_{II} \in \mathbb{C}^{Q \times Q}$ is the impedance matrix between internal pixel ports. $\mathbf{i}_F \in \mathbb{C}^{3 \times 1}$, $\mathbf{i}_I \in \mathbb{C}^{Q \times 1}$ are the current vectors of feeding ports and pixel ports, respectively, and \mathbf{v}_F and \mathbf{v}_I are corresponding voltage vectors. The \mathbf{Z} -matrix of the three feeding ports, denoted as \mathbf{Z}_{PR} , is expressed by [41]

$$\mathbf{Z}_{PR}(\mathbf{x}) = \mathbf{Z}_{FF} - \mathbf{Z}_{FI} [\mathbf{Z}_{II} + \mathbf{Z}^L(\mathbf{x})]^{-1} \mathbf{Z}_{IF}, \quad (31)$$

from which the S-parameters $\mathbf{S}_{PR} \in \mathbb{C}^{3 \times 3}$ of one unit cell can be derived.

Our objective is to ensure that the output current \mathbf{B} of the unit cell aligns with the target $\hat{\mathbf{B}}$ as outlined in Section III. For each feeding port, the outgoing or reflected currents can be found in Fig. 7. Since with all feeding ports well matched, the reflected currents are negligible, i.e., $i_{F,1}^-, i_{F,2}^-, i_{F,3}^- \approx 0$, while the outgoing currents $i_{F,1}^+, i_{F,2}^+, i_{F,3}^+$ play dominant roles. Thus the relationship between the currents at the feeding ports can be described as

$$i_{F,2}^- = S_{21} \cdot i_{F,1}^+, \quad i_{F,3}^- = S_{31} \cdot i_{F,1}^+, \quad (32)$$

where S_{21} and S_{31} are the (2, 1)-th and (3, 1)-th term of \mathbf{S}_{PR} . Therefore, S-parameters can be directly used as optimization goals instead of the output current vector $\mathbf{i}_{M,n}^1$ from (23) or other $i_{n,n}^k$ in the PRBFN topology. In subsequent optimization steps, we only use S-parameters instead of current-based conditions for simplicity.

As a result, the S-parameters obtained in the n -th reconfigurable state should approximate the target current $\hat{\mathbf{i}}_n$ in amplitude and phase as closely as possible. Collecting N vectors $\mathbf{x}_n, \forall n = 1, 2, \dots, N$ into set \mathcal{X} , the optimization

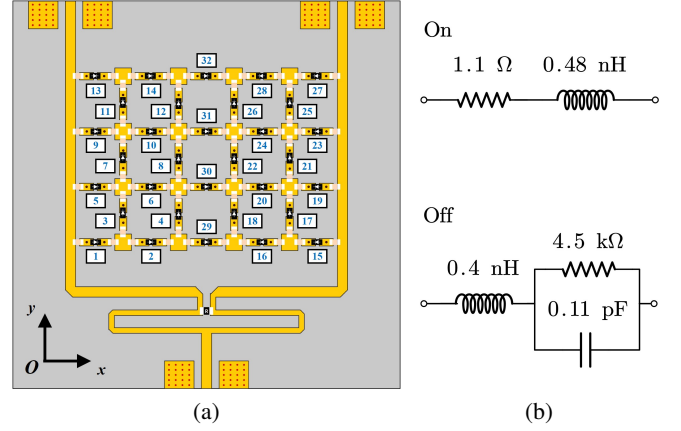


Fig. 8. (a) Top view of the 2-port PRBFN (or unit cell), with $Q = 32$ internal pixel connections. (b) The equivalent circuit model of the PIN diode SMP1345-079LF with its on or off state.

problem for the PRBFN unit cell can be expressed as

$$\begin{aligned} \min_{\mathbf{x}_n \in \mathcal{X}} \max_{f_s} \left\{ \sum_{n=1}^N [c_1 G_1(\mathbf{x}_n, f_s) + c_2 G_2(\mathbf{x}_n, f_s)] \right\}, \\ \text{s.t. } (C1) : \max\{S_{kk,n}(\mathbf{x}_n, f_s)\} < t_s, \quad k = 1, 2, 3, \\ (C2) : \max\{S_{23,n}(\mathbf{x}_n, f_s)\} < t_m, \\ (C3) : \max\{1 - G_3(\mathbf{x}_n, f_s)\} < t_{\text{loss}}, \end{aligned} \quad (33)$$

where c_1, c_2 are weights, (C1) is the constraint of reflection coefficients, (C2) is the constraint of mutual couplings, (C3) is the constraint of energy loss. $t_s = -10$ dB and $t_m = -15$ dB are the thresholds for impedance matching and mutual coupling, and t_{loss} is the threshold for insertion loss. $G_1(\mathbf{x}_n, f_s)$, $G_2(\mathbf{x}_n, f_s)$ measure the amplitude and phase match to the desired $\hat{\mathbf{B}}$, respectively, and $G_3(\mathbf{x}_n, f_s)$ expresses the total transmission power. Taking the unit highlighted by the red box in Fig. 6 as an example again, $G_1(\mathbf{x}_n, f_s)$, $G_2(\mathbf{x}_n, f_s)$, and $G_3(\mathbf{x}_n, f_s)$ can be expanded as

$$\begin{aligned} G_1 &= \left\| \frac{[|S_{21,n}|, |S_{31,n}|]^T}{\sqrt{G_3}} - \frac{[\hat{i}_{1,n}, \hat{i}_{2,n}]^T}{\|\hat{\mathbf{i}}_{M,n}^1\|_2} \right\|_2^2, \\ G_2 &= \left| (\angle S_{21,n} - \angle S_{31,n}) - (\angle \hat{i}_{1,n} - \angle \hat{i}_{2,n}) \right|^2, \\ G_3 &= |S_{21,n}|^2 + |S_{31,n}|^2, \end{aligned} \quad (34)$$

where (\mathbf{x}_n, f_s) is omitted for simplicity. If an internal port, for example, the q -th, remains open-circuited in all N reconfigurable states, the diode at that location can be directly removed, leaving the pixel port open. If, additionally, the port remains short in all states and impedance matching is preserved upon verification, the diode may be replaced with a shorting metal wire. This approach reduces the number of required RF switches, thereby lowering design complexity.

Given the symmetry of the target correlation matrix in Fig. 4, the target $\hat{\mathbf{B}}$ can also be set to exhibit this symmetry. This property allows us to design only half of the reconfigurable states in the PRBFN unit. For instance, state 1 and state N are symmetric, i.e., the outputs at ports 2 and 3 in state 1

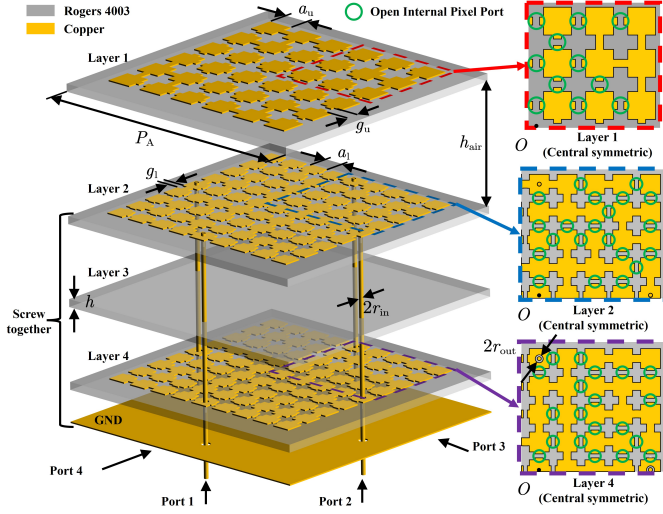


Fig. 9. The configuration of the proposed compact high-isolated 4-port MIMO antenna. Dimensions: $P_A = 75$, $h_{\text{air}} = 8$, $h = 1.524$, $a_u = 7$, $g_u = 3.6$, $a_l = 5$, $g_l = 2$, $r_{\text{in}} = 0.3$, $r_{\text{out}} = 0.6$ (Unit: mm).

correspond to those at ports 3 and 2 in state N , respectively. This symmetry significantly reduces the optimization burden.

Using the four steps described above the PRBFN-FAS can be designed as described in the next section.

IV. FAS PROTOTYPE AND EXPERIMENTAL RESULTS

In this section, we present experimental results for our FAS methodology and PRBFN-FAS designs. In the section that follows, we present results for the performance of our designs in a system setting.

There are three parts to the results we present. First, we provide details of the generic antenna that we utilize in demonstrating the PRBFN structure. The second and third parts are the beamformers and experimental results for 2-port and 4-port PRBFN-FAS designs with $W = 0.5$, $N = 11$ and $N = 1.5$, $N = 18$ respectively.

A. Compact High-Isolated 4-Port MIMO Antenna

As an integral part of the PRBFN-FAS architecture, the MIMO antenna plays a critical role in maintaining high isolation between ports, which ensures that \mathbf{K}_M in formula (12) closely approximates the identity matrix. Before introducing the two examples of PRBFN in the following sections, this section presents the design of a compact, high-isolated, four-port ($N_A = 4$) MIMO antenna intended for radiation in the PRBFN-FAS.

Based on the pixel antenna approach, we design a compact, high-isolated MIMO antenna following established methodologies [41], [42]. The antenna configuration, shown in Fig. 9, consists of a central-symmetric structure excited by four feeding ports. It incorporates three metal pixel layers, with all four feeds connected to the middle layer (Layer 2). Extending the design in [43], we add an upper pixel layer (Layer 1) to enhance bandwidth and a lower pixel layer (Layer 4) to reduce couplings between the 4 feeding ports. The connections between pixels are selected based on optimization using

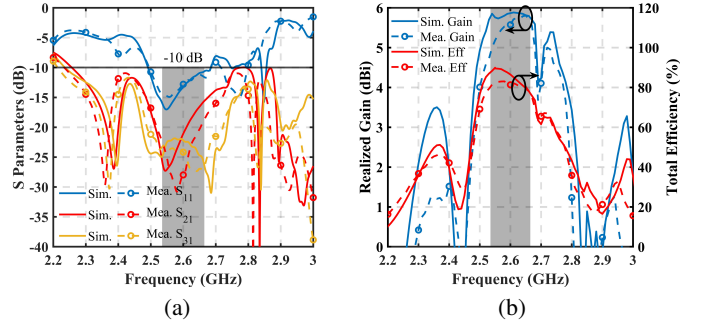


Fig. 10. Simulated and measured (a) S-parameters, (b) efficiency and broadside realized gain of the proposed MIMO antenna.

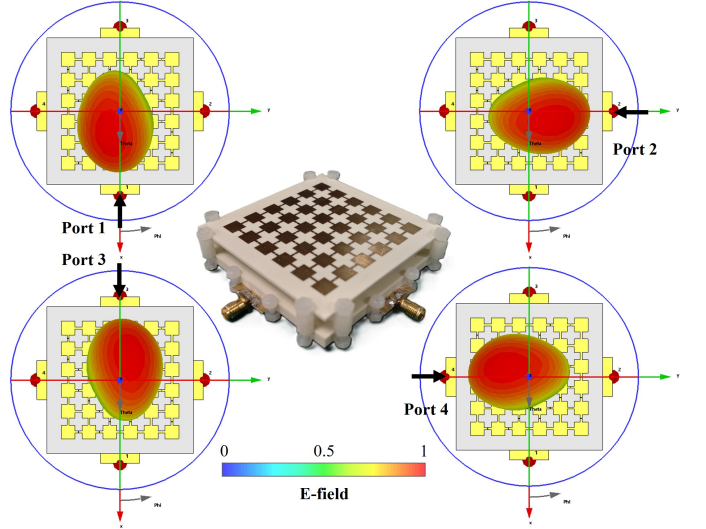


Fig. 11. The prototype of the MIMO antenna, with corresponding normalized 3D radiation patterns at 2.6 GHz for 4 different feeding ports.

established proceeds [41], [42]. The final structure comprises 198 metal pixels and 348 internal pixel ports.

Due to the central-symmetric structure of the proposed MIMO antenna, the S-parameters of all four ports exhibit nearly identical behavior. The simulated and measured S-parameters are presented in Fig 10(a). It can be observed that across the 5% fractional bandwidth at the center frequency of 2.6 GHz, all four ports are well matched, and the mutual couplings between any two ports remain below -20 dB. The realized gain and total efficiency are presented in Fig. 10(b). Within the operating bandwidth, the realized gain exceeds 5 dBi and the radiation efficiency is consistently above 80%. These results demonstrate that our proposed MIMO antenna exhibits excellent performance. Fig. 11 shows the antenna prototype and the radiation patterns when each of the four feeding ports is excited individually. It can be observed that excitation from different ports produces clearly diversified radiation characteristics with favorable broadside radiation performance.

As the radiating terminal of the PRBFN-FAS, the most critical performance metric of the proposed MIMO antenna is that its correlation matrix \mathbf{K}_M must closely approximate the identity matrix \mathbf{U}_{N_A} . This requires orthogonal radiation patterns when exciting the four feed ports. Within the frequency

TABLE I
COMPARISON OF THE PROPOSED MIMO ANTENNA AND PREVIOUS WORKS

Ref.	Port Num.	Freq. (GHz)	Volume (λ_0^3)	Bandwidth (%)	Isolation (dB)
[43]	4	2.435	$0.68 \times 0.68 \times 0.116$	2.05 (-10 dB)	>12
[44]	4	2.2	$1.18 \times 1.18 \times 0.015$	1.4 (-10 dB)	>20
[45]	4	4.15	$0.97 \times 0.97 \times 0.034$	40.96 (-6 dB)	>12
[46]	4	3.89	$1.95 \times 1.3 \times 0.065$	16.2 (-10 dB)	>20
[42]	4	2.55	$0.64 \times 0.64 \times 0.12$	3.55 (-10 dB)	>18
Ours	4	2.6	$0.65 \times 0.65 \times 0.12$	6.5 (-10 dB)	>18

range of 2.52 GHz to 2.68 GHz, the \mathbf{K}_M matrix computed by formula (12) is very close to the identity matrix \mathbf{U}_{N_A} . The maximum off-diagonal element of \mathbf{K}_M within the operating bandwidth is 0.06, indicating near-ideal orthogonality and fully satisfying the requirements of the PRBFN-FAS architecture.

In addition, one of the key features of our proposed MIMO antenna is its ability to achieve high compactness while maintaining high port isolation. As summarized in Table I, which compares our design with several previous compact MIMO antennas with $N_A = 4$ ports, it is generally challenging to realize both wide bandwidth and high isolation without obviously increasing the MIMO antenna size. In contrast, the size of the proposed MIMO antenna is comparable to that of one single antenna with the size of $0.5\lambda_0 \times 0.5\lambda_0$, yet it achieves high isolation across a bandwidth exceeding 5%, underscoring the competitive advantage of our design. In the next two subsections, this 4-port MIMO antenna will be applied in the PRBFN-FAS with $W = 0.5$, $N = 11$ and $N = 1.5$, $N = 18$, respectively.

B. Case 1: 2-Port PRBFN-FAS with $W = 0.5$ and $N = 11$

In the first design, in order to validate the operating principle of the PRBFN-FAS, we begin with the simplest configuration, i.e., a PRBFN comprising only one unit cell with $N_A = 2$ output ports. This corresponds to an equivalent FAS with parameters $W = 0.5$ and $N = 11$.

After optimization, the resulting pixel interconnections and DC bias network distributions are illustrated in Fig. 12(a) and (b), respectively. Among the $Q = 32$ internal pixel ports, 20 are loaded with diodes. The on or off states of these 20 diodes across all $N = 11$ reconfigurable states are summarized in Table II, listed in ascending order according to the number established in Fig. 8(a). It can be observed that the last 4 bits of the binary vectors correspond to the 4 diodes located along the central symmetry axis. The remaining 16 diodes exhibit symmetric states across $N = 11$ reconfigurable states. Same color means the symmetric states.

Considering the mirror symmetry between states 1–5 and states 7–11 with respect to the center symmetry axis, Fig. 13 presents the simulated and measured S-parameters for the first six states. The remaining states (7 to 11) mirror the behavior of states 1 to 5, with identical S-parameters except for a reversal between output ports 2 and 3. As shown, the return losses in all states remains below -10 dB across the operating bandwidth, indicating excellent impedance matching. Isolation between the two output ports exceeds 20 dB throughout the band.

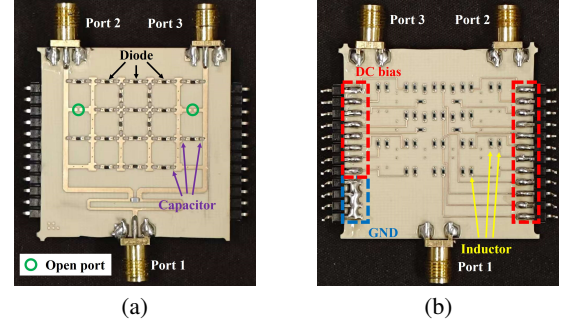


Fig. 12. The 2-port PRBFN prototype. (a) Top and (b) bottom view. Among the $Q = 32$ internal pixel ports, 20 are loaded with diodes. The pixel ports in green circles are open.

TABLE II
STATES OF DIODES IN $N = 11$ RECONFIGURABLE STATES

No.	States of 20 diodes	No.	States of 20 diodes
1	1010 1011 0011 1001 0010	2	1010 0011 0110 1101 0000
3	1010 1111 0111 1101 1100	4	1011 1011 0111 1100 0001
5	0111 0000 0011 1001 0110	6	0110 0000 0110 1100 0101
7	0011 1001 0111 0000 0110	8	0111 1100 1011 1011 0001
9	0111 1101 1010 1111 1100	10	0110 1101 1010 0011 0000
11	0011 1001 1010 1011 0010		

Simulated and measured results for transmission coefficients, S_{21} and S_{31} , show strong agreement, validating the accuracy of the proposed design methodology.

To achieve the target Bessel correlation (14), the phase difference between output ports is critical. Fig. 14(a) illustrates the measured phase difference between the two output ports. The black dots at 2.6 GHz depict the ideal phase difference specified in $\hat{\mathbf{B}}$. As shown, the simulated and measured results agree closely across the operating bandwidth, with the phase difference remaining stable. Combined with the consistent output amplitude observed in Fig. 13, the PRBFN maintains stable performance over the entire target bandwidth. Furthermore, the deviation between the measured phase difference and the ideal value in $\hat{\mathbf{B}}$ is within 10° , demonstrating the high accuracy of our design. In addition, the simulated and measured insertion loss of the PRBFN is depicted in Fig. 14(b). It can be observed that, despite the integration of 20 diodes, the insertion loss remains below 1.8 dB for all reconfigurable states across the 5% operating bandwidth.

Based on the measured outputs of the PRBFN and under the assumption of an ideal antenna ($\mathbf{K}_M = \mathbf{U}_2$) connected to its output, the correlation of the 2-port PRBFN can be derived using formula (13). As illustrated in Fig. 15(a), the measured correlation matrix of N reconfigurable states at 2.6 GHz is given as an example. To quantify the deviation between $\hat{\mathbf{C}}$ and \mathbf{C}_{obj} , formula (21) is modified and the relative error ϵ can be found as

$$\epsilon = \frac{\|\mathbf{C} - \mathbf{C}_{\text{obj}}\|_F^2}{f_1(\hat{\mathbf{B}}')} = \frac{\|\mathbf{C} - \mathbf{C}_{\text{obj}}\|_F^2}{|||(\hat{\mathbf{B}}')^H \hat{\mathbf{B}}' - \mathbf{C}_{\text{obj}}\|_F^2}, \quad (35)$$

where $||(\hat{\mathbf{B}}')^H \hat{\mathbf{B}}'|$ is an all-one matrix. Across the 5% bandwidth, $\epsilon = 0.051, 0.045, 0.055$ at 2.55 GHz, 2.6 GHz, 2.65 GHz, respectively. The low relative errors demonstrate that the measured correlation results exhibit strong agreement with

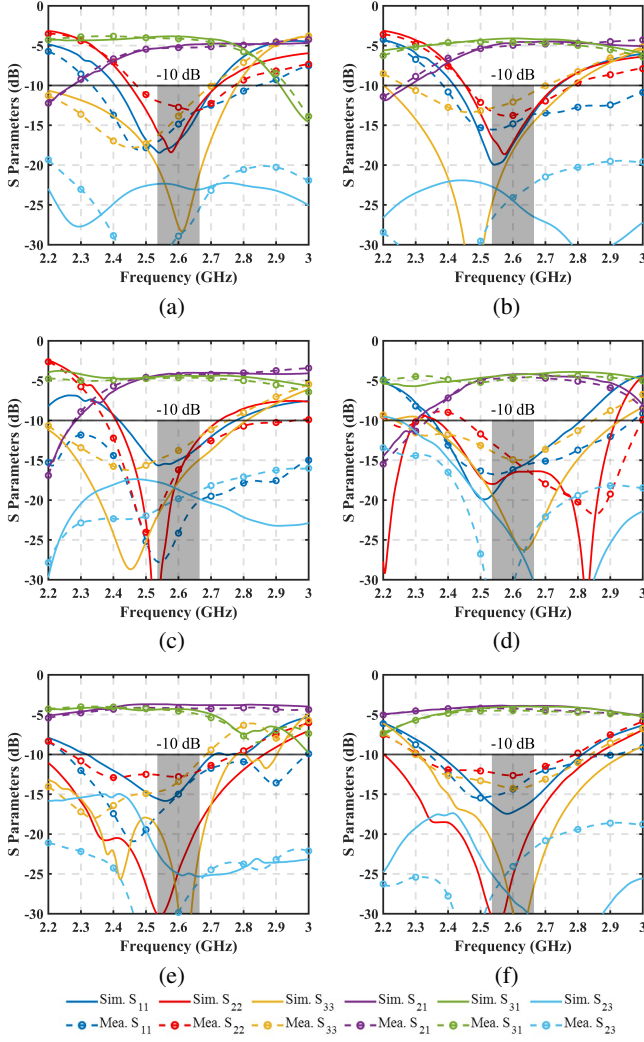


Fig. 13. Simulated and measured S-parameters of the proposed 2-port PRBFN (a)-(f) State 1 to 6. States 11 to 7 mirror States 1 to 5 with the two output ports interchanged.

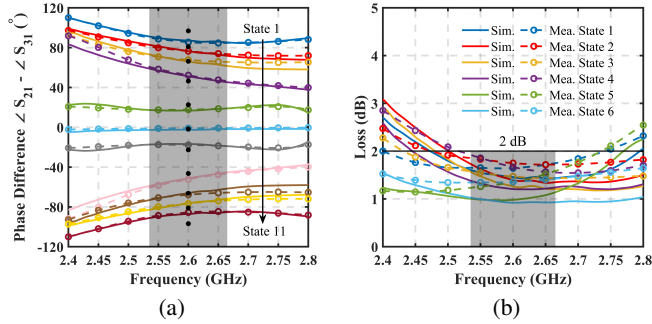


Fig. 14. (a) Simulated and measured phase difference between 2 output ports. The black dots are the phase difference of the target $\hat{\mathbf{B}}$. (Solid line: simulated. Dashed line: measured.) (b) Simulated and measured insertion loss.

both the ideal Bessel correlation \mathbf{C}_{obj} shown in Fig. 4(a) and the target correlation $\hat{\mathbf{C}}$ calculated by $\hat{\mathbf{B}}$ given in Fig. 4(c).

Utilizing the unit cell described in the previous section, we integrated it with the compact four-port high-isolated MIMO antenna (using only 2 of its ports) proposed above to evaluate the overall radiation performance of the PRBFN-FAS. The test setup is illustrated in Fig. 16(a), where the

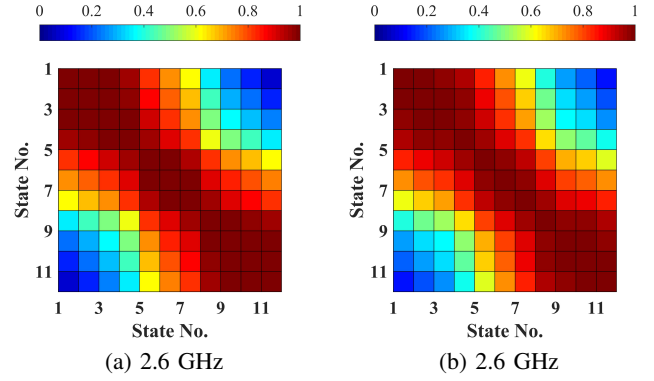


Fig. 15. Measured correlation of N reconfigurable states (a) of the independent 2-port PRBFN with idea antenna whose $\mathbf{K}_M = \mathbf{U}_2$, and (b) of PRBFN-FAS including the 2-port PRBFN and the proposed MIMO antenna. Correlation remains stable across the desired 5% bandwidth. At 2.55, 2.6, 2.65 GHz, the relative errors are $\epsilon = 0.051, 0.045, 0.055$ for (a) and $\epsilon = 0.047, 0.047, 0.052$ for (b), respectively.

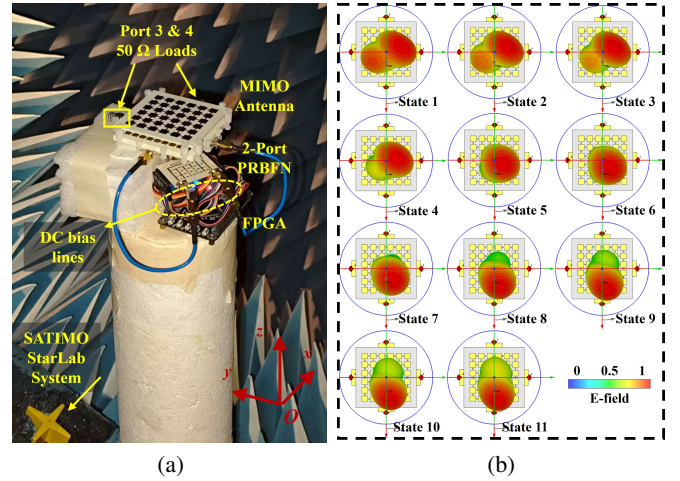


Fig. 16. (a) Measurement setup of the 2-port PRBFN-FAS. (b) Measured radiation pattern of $N = 11$ reconfigurable states.

reconfiguration of the PRBFN-FAS is controlled via an FPGA. Fig. 16(b) presents the measured 3D radiation patterns across all $N = 11$ reconfigurable states. Radiation patterns in adjacent states exhibit strong similarity, consistent with the high correlation property $C_{i,j} \approx 1$. In contrast, patterns from states far apart show significant variation, demonstrating high orthogonality with $C_{i,j} \approx 0$. The measured correlation matrix for $N = 11$ beamforming radiation patterns \mathbf{C} is shown in Fig. 15(b), which aligns closely with the results obtained from the standalone PRBFN characterization. The measured correlation of the 2-port PRBFN-FAS shows very low relative errors, where $\epsilon = 0.047, 0.047$, and 0.052 at 2.55 GHz, 2.6 GHz, and 2.65 GHz, respectively. These minimal deviations demonstrate remarkable stability across the desired 5% operating bandwidth.

It is worth noting that the proposed PRBFN-FAS indeed exhibits beam-scanning capabilities. However, the primary focus lies not on the specific direction of each radiation pattern, but on the relationships among all reconfigurable states. In essence, this approach can be viewed as a form of dense sampling in the radiation pattern domain, which effectively

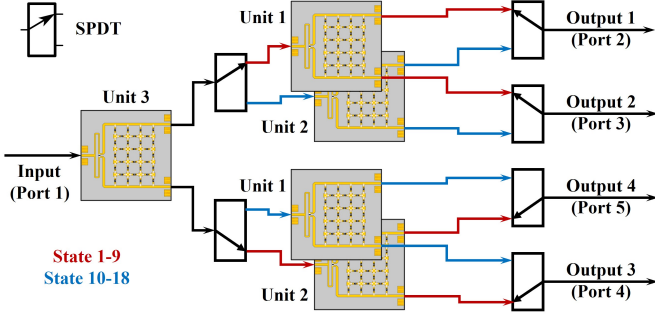


Fig. 17. Architecture of the proposed 4-port PRBFN, where the Unit 1, 2, and 3 are the unit cell given in Fig. 7 but with various configurations.

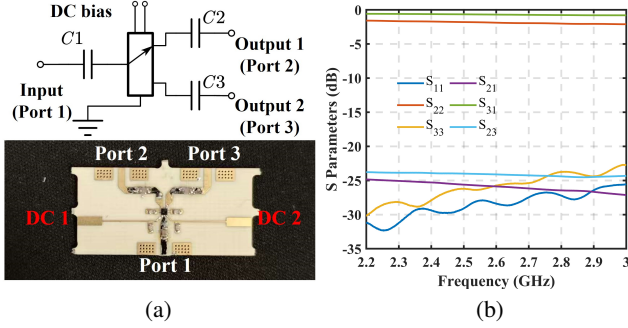


Fig. 18. (a) Circuit model and prototype of the SPDT, with $C1, C2, C3 = 100$ pF. (b) The measured S-parameters of the SPDT when it is switched to port 3 (output 2).

corresponds to dense spatial sampling. Thereby, the PRBFN-FAS achieves functional equivalence to a conventional FAS.

C. Case 2: 4-Port PRBFN-FAS with $W = 1.5$ and $N = 18$

In the design of Case 1, we validated the feasibility of a 2-port PRBFN using one unit cell. In this section, we extend the PRBFN topology to implement four output ports via a two-stage cascaded structure. The resulting PRBFN-FAS emulates an ideal FAS with parameters $W = 1.5$ and $N = 18$. Supporting $N = 18$ reconfigurable states imposes significant pressure on the second stage, particularly on the reconfigurable unit introduced in Fig. 7. While one approach is to scale the unit cell size and increase the number of reconfigurable pixels and internal pixel ports, we adopt a more efficient strategy, reusing the same compact unit from Fig. 7 combined with single-pole double-throw (SPDT) switches to reduce the reconfiguration burden for each unit. The architecture of the 4-port PRBFN is illustrated in Fig. 17.

The circuit schematic and physical prototype of the SPDT switch are depicted in Fig. 18(a). By adjusting the DC bias voltages, the SPDT can be configured to select between its two output ports. Fig. 18(b) presents the S-parameters when output 2 is selected, demonstrating excellent impedance matching and low insertion loss of approximately 0.7 dB. Since the phase difference between output ports is critical, the topology in Fig. 17 ensures an identical number of SPDTs are inserted in each RF signal path. This symmetric arrangement minimizes any potential impact on phase differences, thereby preserving the optimization method of the PRBFN.

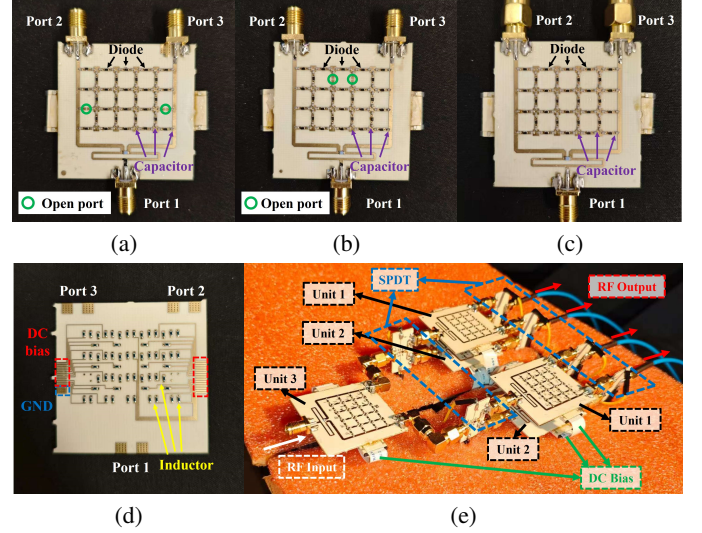


Fig. 19. Top view of (a) Unit 1, (b) Unit 2, and (c) Unit 3. (d) The DC feeding layer. (e) The overall prototype of 4-port PRBFN, including two Unit 2, two Unit 3, one Unit 1, and six SPDTs.

Leveraging the symmetry of the target correlation matrix $\hat{\mathbf{C}}$ in Fig. 4(d), the first stage of the PRBFN (Unit 3) only needs to support $N/2$ reconfigurable states, as the remaining $N/2$ states can be achieved through mirroring the configurations of diode states. Thus, SPDTs are applied solely in the second stage to manage the expansion of reconfigurable states without increasing unit complexity. Following the established design methodology in Section III, the design steps of the 4-port PRBFN include

1. Calculate the target for Unit 1 and Unit 2, written as $\hat{\mathbf{I}}_1$ and $\hat{\mathbf{I}}_2$. Since each unit only supports $N/2 = 9$ reconfigurable states, the target current $\hat{\mathbf{B}}$ of 4 ports can be equally split into $\hat{\mathbf{B}} = [\hat{\mathbf{I}}_1, \hat{\mathbf{I}}_2]$, each with $N_A = 4$ rows and $N/2 = 9$ columns.
2. Optimize the configurations of Unit 1 and Unit 2 using (33). Therefore, $\mathbf{i}_{2,n}^1$ can be calculated by normalization, enabling $\|\mathbf{i}_{2,n}^1\|_2^2 = 1, \forall n = 1, 2, \dots, N$, and then $\mathbf{i}_{2,n}^2$ can be obtained through mirroring, e.g. $\mathbf{i}_{2,n}^1 = \mathbf{i}_{2,N-n+1}^2$.
3. The target current of Unit 3 can be derived via equation (29) with the optimized results from last two steps.
4. (33) is applied again to optimize the configuration of Unit 3, thereby completing the full iterative design process.

The configurations of the three reconfigurable units are given in Fig. 19(a)-(c), and the final 4-port PRBFN prototype is depicted in Fig. 19(e).

The simulated and measured transmission coefficients, including $S_{21}, S_{31}, S_{41}, S_{51}$, of the nine states in the 4-port PRBFN are plotted in Fig. 20(a) to (i), respectively. Both simulation and measurement results show strong agreement in magnitude across the central 5% fractional bandwidth. Fig. 20(j) summarizes the total transmission loss of the 4-port PRBFN, which includes a fixed 1.4 dB loss from the two SPDTs including in each RF signal path. The maximum loss introduced by two cascaded units across all reconfigurable states is approximately 5.3 dB, which can be readily compensated by the four amplifiers in the subsequent stage in Fig.

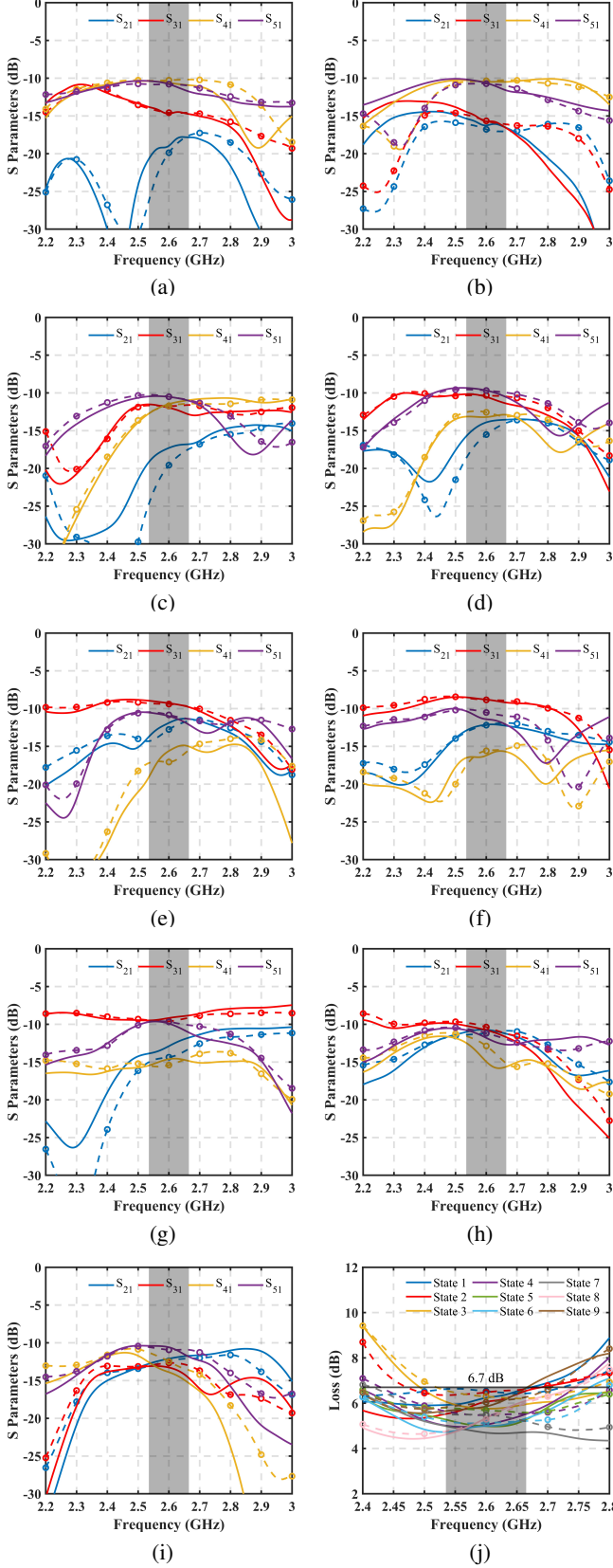


Fig. 20. $S_{21}, S_{31}, S_{41}, S_{51}$ of the proposed 4-port PRBFN (a)-(i) State 1 to 9. States 18 to 10 mirror States 1 to 9 with the four output ports interchanged. (j) Insertion losses. (Solid lines: simulated. Dash lines: measured.)

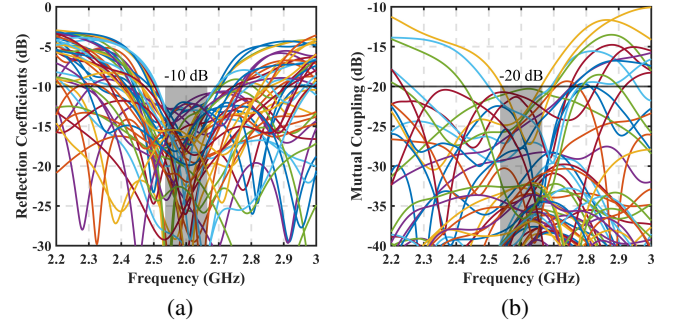


Fig. 21. Measured (a) reflection coefficients ($S_{11}, S_{22}, S_{33}, S_{44}, S_{55}$), and (b) mutual couplings ($S_{23}, S_{24}, S_{25}, S_{34}, S_{35}, S_{45}$) of the 4-port PRBFN across all $N = 18$ reconfigurable states.

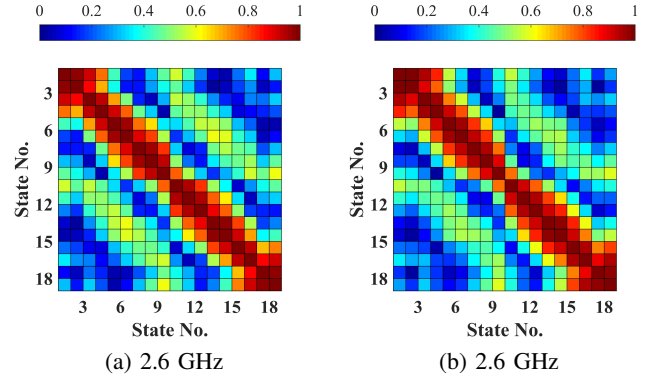


Fig. 22. Measured correlation of N reconfigurable states (a) of the independent 4-port PRBFN with ideal antenna whose $\mathbf{K}_M = \mathbf{U}_4$, and (b) of PRBFN-FAS including the 4-port PRBFN and the proposed MIMO antenna. Correlation remains stable across the desired 5% bandwidth. At 2.55, 2.6, 2.65 GHz, the relative errors are $\epsilon = 0.057, 0.043, 0.037$ for (a) and $\epsilon = 0.062, 0.041, 0.035$ for (b), respectively.

2. The reflection coefficients and mutual coupling for all five external ports across all 18 reconfigurable states are presented in Fig. 21(a) and (b), respectively. Within the desired central 5% operating bandwidth, the reflection coefficients remain below -10 dB and the mutual coupling is always below -20 dB, confirming excellent impedance matching and high port isolation in the proposed design.

With an ideal MIMO antenna whose $\mathbf{K}_M = \mathbf{U}_4$, the pattern correlation can be calculated by the measured transmission coefficients of the 4-port PRBFN using formula (13). As shown in Fig. 22(a), the correlation relationship at 2.6 GHz agrees well with both ideal Bessel correlation \mathbf{C}_{obj} in Fig. 4(b) and the target correlation $\hat{\mathbf{C}}$ derived from $\hat{\mathbf{B}}$ in Fig. 4(d). The relative errors at 2.55GHz, 2.6 GHz, and 2.65 GHz are $\epsilon = 0.057, 0.043, 0.037$, which are small enough to provide consistency.

Following Case 1 in the last subsection, the proposed 4-port PRBFN was connected to the 4-port compact MIMO antenna, and the radiation patterns of the overall PRBFN-FAS were measured. The test setup, shown in Fig. 23(a), employed three FPGAs to control the reconfigurable state switching. The measured radiation patterns for all $N = 18$ states are presented in Fig. 23(b). As expected, patterns corresponding to adjacent states exhibit strong similarity, while those from widely separated states demonstrate clear orthogonality. The

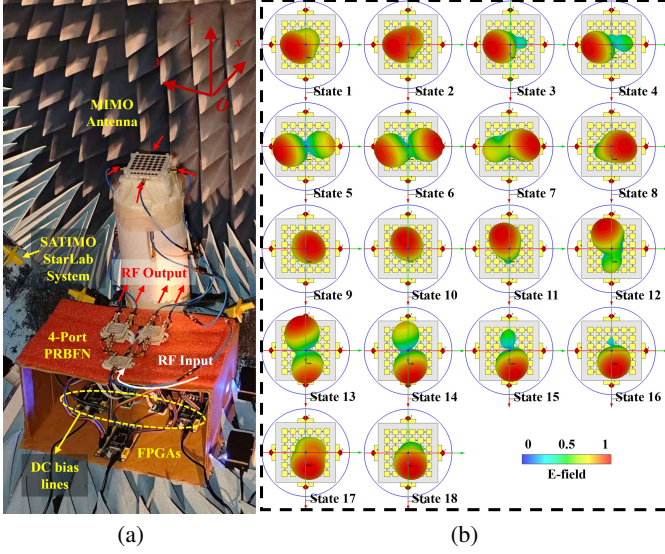


Fig. 23. (a) Measurement setup of the 4-port PRBFN-FAS. (b) Measured radiation pattern of $N = 18$ reconfigurable states.

resulting correlation matrix \mathbf{C} of the $N = 18$ beamforming reconfigurable radiation patterns, illustrated in Fig. 23(b), shows excellent agreement with the correlation performance obtained from the standalone 4-port PRBFN in Fig. 23(a). From 2.55 GHz to 2.65 GHz, the relative errors ($\epsilon = 0.062, 0.041, 0.035$) are sufficiently small, demonstrating both high accuracy to \mathbf{C}_{obj} and high stability across the bandwidth.

V. SYSTEM EXPERIMENTS AND RESULTS

In the preceding sections, we have validated the correlation performance among reconfigurable states (FAS ports) of the PRBFN-FAS through radiation patterns. This section presents the system-level experiments and evaluation of the proposed 4-port PRBFN-FAS within practical communication systems.

We measure the variations in PRBFN-FAS channels across various PRBFN-FAS states in a rich scattering environment. A MIMO testbed [47] is utilized, which can provide measurements of 4×4 wireless channels every 0.01s. In FAS channel testing, a simplified 2×2 MIMO configuration is utilized. As shown in Fig. 24(a), the Tx side of the test setup consists of the proposed 4-port PRBFN-FAS (Tx 1) and a reference dipole antenna (Tx 2). The dipole serves to monitor channel stability during measurements. Since it is impractical to measure all FAS port channels simultaneously, we instead sequentially scan through the $N = 18$ reconfigurable states of the PRBFN-FAS while ensuring channel stability. Under stable conditions, the channels corresponding to all N FAS ports can be considered quasi-static and thus approximately equivalent at any given time instant. Fig. 24(b) depicts the scheme of the Rx, where both dipoles are set far apart for independence.

The measured channel elements of the MIMO system are denoted as $h_{u,v}$ where u refers to the receiver antenna index and v the transmitter antenna index. Therefore, with both sides equipped with dipoles, $h_{1,2}$ and $h_{2,2}$ are set as benchmark channels which are expected to remain stable.

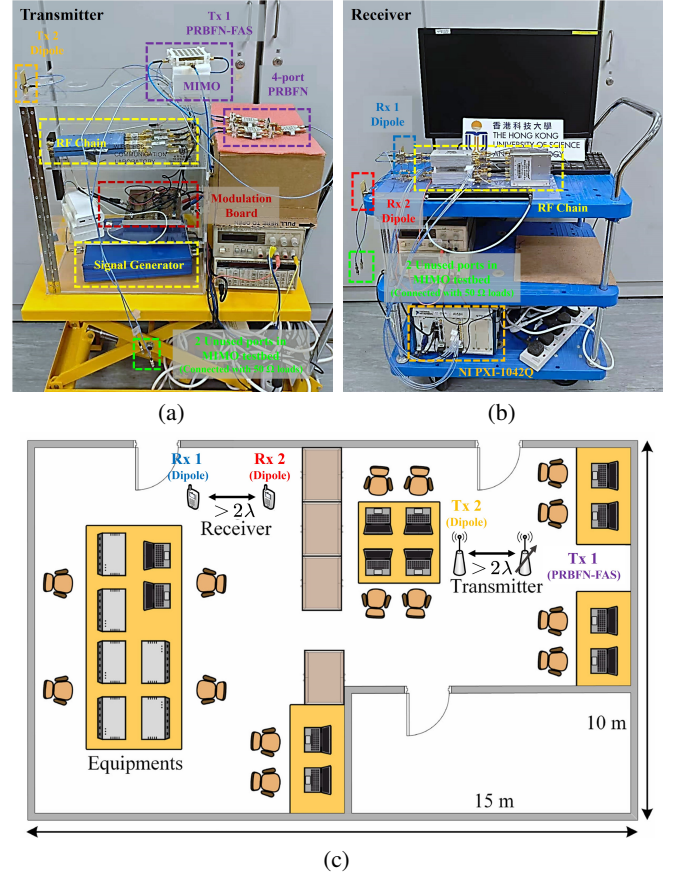


Fig. 24. System experiments setup with the proposed 4-port PRBFN-FAS. (a) Tx of the MIMO testbed, equipped with the 4-port PRBFN-FAS. (b) Rx of the MIMO testbed. (c) Indoor testing environment.

Channels $h_{1,1}, h_{2,1}$ are two FAS channels with the PRBFN-FAS at the Tx side. The PRBFN-FAS is controlled by FPGAs and set to cycle through $N = 18$ reconfigurable states in order, with the switching synchronized to the sampling rate of the MIMO testbed. The channel measurements were conducted in the Wireless Communication Laboratory at the Hong Kong University of Science and Technology. The indoor environment, shown in Fig. 24(c), features non-line-of-sight (NLoS) environments with the Tx and Rx separated by at least 5 meters and obstructed by 2-meter-high cupboards blocking the line-of-sight (LoS) path.

Fig. 25 illustrates the variation in measured channel gains of $h_{1,1}$ and $h_{2,1}$ across different PRBFN-FAS states, corresponding to various FAS ports, evaluated at four distinct spatial locations shown in Fig. 24(c). The results indicate that the PRBFN-FAS generates obvious antenna diversity at various tested locations. Furthermore, in the FAMA case, both users at Rx consistently achieve SIR exceeding 10 dB by switching between FAS ports. The observed variation in signal strength with port switching confirms the effectiveness of the PRBFN-FAS design in practical communication systems.

Based on the channel measurement results, the correlation between different states of the PRBFN-FAS can be evaluated using the averaged autocorrelation coefficient derived from channel measurements collected from $U = 2$ users at K

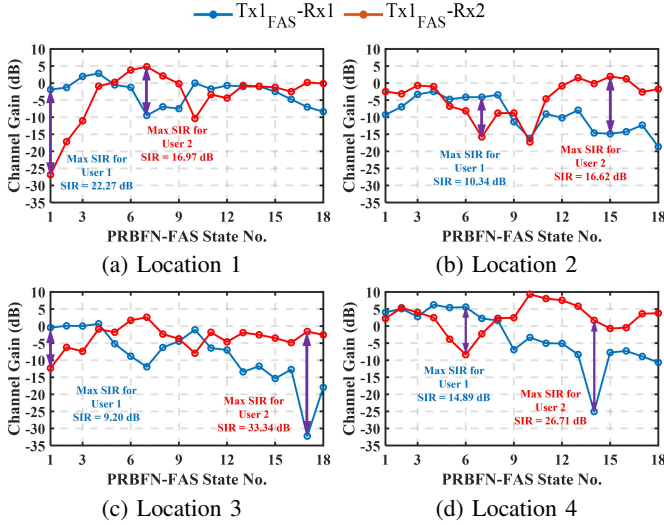


Fig. 25. Measured stationary channels for $N = 18$ PRBFN-FAS ports, with two users (Rx) at (a)-(d) 4 different locations in Fig. 24(c). The optimal FAS ports with largest SIR are marked for each user in FAMA.

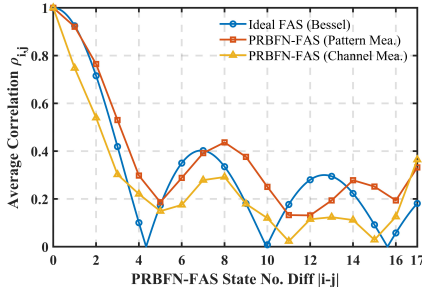


Fig. 26. Correlation of the 4-port PRBFN-FAS reconfigurable states, including measurement results by N radiation patterns (Fig. 22) and practical communication system.

various locations. The measured correlation can be written as

$$C_i^{\text{mea}} = \frac{1}{UK} \sum_{k=1}^K \sum_{u=1}^U \frac{\mathcal{R}(i, u, k)}{\sigma^2(i, u, k)}, \quad (36)$$

where $\mathcal{R}(\cdot)$ is the auto-correlation function, and σ^2 is the standard deviation used for normalization. Collecting all FAS port numbers into a set $\mathcal{V} = \{1, 2, \dots, N\}$, these terms in (36) can be expanded by

$$\begin{aligned} \mathcal{R}(i, u, k) &= \sum_{j, i+j \in \mathcal{V}} h_{u,1}^{(k)}(j) h_{u,1}^{(k)*}(i+j), \\ \sigma^2(i, u, k) &= \sum_{j, i+j \in \mathcal{V}} \|h_{u,1}^{(k)}(j)\|_2 \cdot \|h_{u,1}^{(k)}(i+j)\|_2, \end{aligned} \quad (37)$$

where $h_{u,1}^{(k)}(j)$ represents the measured channel between the u -th Rx and the PRBFN-FAS at Tx 1 with its j -th state at location k . The average correlation by measured channels is depicted in Fig. 26(a), where the correlation by radiation patterns \mathcal{C} and ideal Bessel curve \mathcal{C}_{obj} are plotted for comparison. It can be observed that the correlation performance obtained through the communication system exhibits strong consistency with previous results. The deviations can be attributed to the non-ideal scatterings of the actual test environment [20].

VI. DISCUSSIONS

In this section, we provide further discussions on several issues in our proposed PRBFN-FAS design.

A. Advantages of PRBFN over conventional BFN

In this design, the PRBFN architecture is adopted due to its high reconfigurability, which is able to support the large number of reconfigurable states N required by FAS. The core principle involves precisely controlling the outputs of the PRBFN to satisfy the specific beamforming criteria. Therefore, a question arises: whether a traditional BFN could be used in place of the PRBFN.

While theoretically feasible, existing BFN implementations face practical limitations. For instance, the BFNs in [25], [26] provides discrete control in amplitude and phase. However, as shown in Fig. 14(a), approaching the ideal values specified in $\hat{\mathbf{B}}$ would require this discrete design to achieve a phase accuracy of at least 5 bits, which is hard to achieve with PCB techniques. Meanwhile, for lower-frequency applications like 2.6 GHz, implementing high-precision phase shifters using solid-state circuits demands considerable chip area, making such solutions prohibitively expensive [48], [49].

Another example is the BFN proposed in [27], which offers two output ports with independently and continuously tunable amplitude and phase differences. With careful design, such a BFN could emulate the functionality of our PRBFN. However, this approach introduces considerable practical challenges. The BFN reconfigurability in [27] relies on 6 varactor diodes for one unit cell, necessitating many high-precision linear power supplies or digital-to-analog converters (DACs) for accurate control. This approach is far more complex than the switching diodes directly controlled using digital signals in our PRBFN-FAS. Moreover, as the BFN in [27] was not optimized for FAS applications, it exhibits relatively higher insertion loss since our PRBFN-FAS is specifically designed for FAS applications.

In contrast, the PRBFN proposed in this work is specifically optimized for FAS requirements. Its reconfigurable output closely approximates the target $\hat{\mathbf{B}}$ while maintaining relatively low insertion loss. Moreover, the use of diode-based reconfiguration enables straightforward direct control via FPGAs. These advantages establish the PRBFN as a superior alternative to conventional BFN for FAS implementations.

B. Applications of PRBFN-FAS in Rx

In the PRBFN-FAS architecture illustrated in Fig. 2, the low-power RF signal, after passing through the PRBFN, is amplified by PAs with minimal distortion, making the PRBFN-FAS well-suited for Tx applications. However, when employed at the Rx side, the insertion loss of the PRBFN can degrade the SNR, potentially limiting its performance. To overcome this, low-noise amplifiers (LNAs) must be deployed for PRBFN-FAS applications at Rx. N_A LNAs are connected after N_A antenna ports, and the LNA outputs feed the proposed PRBFN.

TABLE III
COMPARISON OF THE PROPOSED PRBFN-FAS AND OTHER EARLY ATTEMPTED FAS ANTENNAS IN PREVIOUS WORKS

Ref.	Method	Freq. (GHz)	Port Num. N	FAS Size $W\lambda_0$	Port Density N/W	Bandwidth (%)	Radiation Eff. (%)	Switching Speed	Scalability	Control	Tx/Rx
[14]	Motor	3.5/27.5	600/100	6/5	100/20	N.A.	N.A.	very slow	poor	motor	Both
[16]	Liquid Metal	27	continuous	1	≥ 12	20	80	$\geq 1s$	moderate	pump	Both
[20]	PRA	2.5	12	0.5	24	2	70	$< 1\mu s$	hard	FPGA	Rx
[19]	Meta-fluid	26.5	15 \times 8	6.6 \times 2.6	2.3 \times 3	3.8	N.A.	$< 1\mu s$	easy	FPGA	Rx
Ours	2-port PRBFN	2.6	11	0.5	22	7.7	90	$< 1\mu s$	moderate	FPGA	Both
Ours	4-port PRBFN	2.6	18	1.5	12	5	90	$< 1\mu s$	moderate	FPGA	Both

• To support FAS with high performance, fast switching speed (≤ 1 ms) and a port density $N/W > 10$ are required.

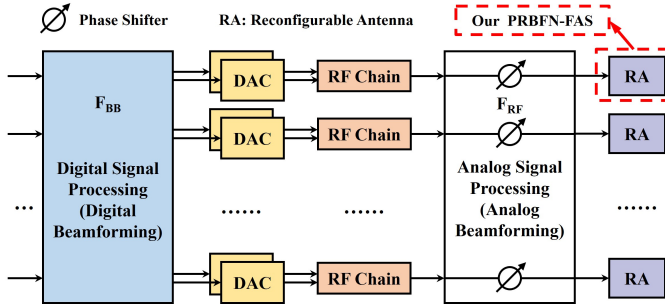


Fig. 27. Tri-hybrid MIMO architecture integrated with digital beamforming, analog beamforming, and EM beamforming by reconfigurable antennas (RAs). Our proposed PRBFN-FAS design actually serves as RAs, which can cooperate with the traditional digital and analog beamforming.

C. Comparison with previous FAS designs

For practical FAS implementations, various hardware architectures have been proposed in previous works. This subsection reviews existing FAS hardware designs and compares them with our proposed PRBFN-FAS architecture, highlighting the advantages of our approach. A detailed comparison is provided in Table III, which incorporates the reference data from [50].

A comparative analysis reveals distinct trade-offs among existing FAS hardware implementations. Designs based on physical movement achieve nearly continuous port switching but are severely limited by low switching speeds. Alternatively, rapidly switchable architectures such as PRA-FAS and meta-fluid FAS face challenges in Tx applications due to the non-linearity of reconfigurable components [23]. These approaches also exhibit inherent limitations: the former suffers from limited scalability of size, while the latter is constrained by low FAS port density, which ultimately restricts performance of FAS.

In contrast, the PRBFN-FAS proposed in this work achieves a port density (N/W) exceeding 10, μs -level switching speed, and maintains signal integrity in Tx operation. Furthermore, the design methodology ensures scalable deployment. The comparative advantages of PRBFN-FAS are demonstrated through these performance metrics and architectural features.

D. Implicit Beamforming Principle in PRA-FAS

It should be noted that the PRA-FAS design in [20] implicitly employs beamforming principles, though this remains entirely masked under its complex optimization process and

is not explicitly discussed in the original work. Using the proposed theory in this work, the PRA-FAS contains several orthogonal radiation components, where identity matrix \mathbf{K}_M arises naturally. Optimizing its N reconfigurable pixel connections corresponds to controlling the N proportions of these components, and these correspond to the beamforming currents \mathbf{B} in Fig. 2. Similarly, the settings of these N reconfigurable pixels can be optimized to approximate Bessel function correlation C_{obj} . However, [20] operates purely through numerical optimization without introducing any explicit beamforming concept. In contrast, the method proposed in this paper offers a more intuitive and transparent interpretation of beamforming theory for enabling FAS.

E. Compatibility with Existing Beamforming Techniques

In the theoretical analysis presented in this paper, we establish that pattern-domain FAS can be interpreted through a beamforming framework. While recent research has explored various beamforming implementations for FAS [51]–[53], our method operates at the antenna level and remains fully compatible with conventional array-level beamforming techniques.

To clarify this distinction, we consider the emerging tri-hybrid MIMO architecture [54], which integrates digital beamforming, analog beamforming, and electromagnetic (EM) beamforming implemented through reconfigurable antennas (RAs). Traditional beamforming methods, such as digital beamforming and analog beamforming, operate at the array level and have been the focus of recent FAS-related studies [51]–[53]. In contrast, the PRBFN-FAS proposed in this work acts as one RA element, and can therefore be incorporated into larger array-level beamforming systems without conflict. This positions PRBFN-FAS as a complementary rather than competing technology in beamforming using FAS.

VII. CONCLUSION

This paper has presented a novel PRBFN-FAS architecture capable of high-speed reconfiguration and high-power operation, making it particularly suitable for Tx applications in FAS. Theoretically, we have established that FAS can be interpreted as beamforming in the radiation pattern domain, where traditional FAS port switching corresponds to switching beamforming reconfigurable radiation patterns in the PRBFN-FAS framework. A systematic design methodology has been

introduced for the PRBFN-FAS, along with a scalable expansion approach that supports FAS implementations with different parameter sets.

To validate the proposed design, two PRBFN-FAS prototypes were developed targeting FAS configurations with parameters $W = 0.5$, $N = 11$, $N_A = 2$ and $W = 1.5$, $N = 18$, $N_A = 4$. By controlling the states of integrated diodes, the PRBFN dynamically adjusts the pixel interconnections to achieve the desired amplitude and phase distribution across output ports. Measured results confirm that the PRBFN-FAS achieves a bandwidth exceeding 5%, with S parameters, radiation pattern correlation, and communication performance all aligning closely with theoretical expectations. Experimental deployments in real communication scenarios further verified its robust operation under practical scattering conditions, demonstrating expected correlation behavior, channel capacity, and enhancement of multiple access.

Furthermore, the PRBFN-FAS exhibits strong compatibility with conventional beamforming techniques, enabling its integration into MIMO and hybrid beamforming architectures. By effectively establishing a connection between the diversity of the traditional FAS spatial domain and the diversity of the radiation pattern domain, the PRBFN-FAS offers a scalable, hardware-efficient pathway toward practical high-performance FAS implementations.

DATA AVAILABILITY

The E-field data of the two PRBFN-FAS examples are available at <https://github.com/ZhangJichen2001>. We encourage researchers in related fields of wireless communication to use these results.

REFERENCES

- [1] I.-R. M.2160-0, "Framework and overall objectives of the future development of imt for 2030 and beyond," *ITU-R Recommendation M.2160.0*, 11, 2023.
- [2] W. Saad, M. Bennis, and M. Chen, "A vision of 6G wireless systems: Applications, trends, technologies, and open research problems," *IEEE Network*, vol. 34, no. 3, pp. 134–142, 2020.
- [3] C.-X. Wang, X. You, X. Gao, X. Zhu, Z. Li, C. Zhang, H. Wang, Y. Huang, Y. Chen, H. Haas, J. S. Thompson, E. G. Larsson, M. D. Renzo, W. Tong, P. Zhu, X. Shen, H. V. Poor, and L. Hanzo, "On the road to 6G: Visions, requirements, key technologies, and testbeds," *IEEE Communications Surveys and Tutorials*, vol. 25, no. 2, pp. 905–974, 2023.
- [4] E. G. Larsson, O. Edfors, F. Tufvesson, and T. L. Marzetta, "Massive MIMO for next generation wireless systems," *IEEE Communications Magazine*, vol. 52, no. 2, pp. 186–195, 2014.
- [5] K.-K. Wong, A. Shojaeifard, K.-F. Tong, and Y. Zhang, "Fluid antenna systems," *IEEE Transactions on Wireless Communications*, vol. 20, no. 3, pp. 1950–1962, 2021.
- [6] W. K. New, K.-K. Wong, H. Xu, C. Wang, F. R. Ghadi, J. Zhang, J. Rao, R. Murch, P. Ramirez-Espinosa, D. Morales-Jimenez, C.-B. Chae, and K.-F. Tong, "A tutorial on fluid antenna system for 6G networks: Encompassing communication theory, optimization methods and hardware designs," *IEEE Communications Surveys & Tutorials*, vol. 27, no. 4, pp. 2325–2377, 2025.
- [7] E. Björnson, E. G. Larsson, and M. Debbah, "Massive MIMO for maximal spectral efficiency: How many users and pilots should be allocated?" *IEEE Transactions on Wireless Communications*, vol. 15, no. 2, pp. 1293–1308, 2016.
- [8] E. Nayeri, A. Ashikhmin, T. L. Marzetta, H. Yang, and B. D. Rao, "Precoding and power optimization in cell-free massive MIMO systems," *IEEE Transactions on Wireless Communications*, vol. 16, no. 7, pp. 4445–4459, 2017.
- [9] K.-K. Wong and K.-F. Tong, "Fluid antenna multiple access," *IEEE Transactions on Wireless Communications*, vol. 21, no. 7, pp. 4801–4815, 2022.
- [10] K.-K. Wong, K.-F. Tong, Y. Shen, Y. Chen, and Y. Zhang, "Bruce lee-inspired fluid antenna system: Six research topics and the potentials for 6G," *Frontiers in Communications and Networks*, vol. 3, 2022. [Online]. Available: <https://www.frontiersin.org/articles/10.3389/frcmn.2022.853416>
- [11] J. Zou, H. Xu, C. Wang, L. Xu, S. Sun, K. Meng, C. Masouros, and K.-K. Wong, "Shifting the ISAC trade-off with fluid antenna systems," *IEEE Wirel. Commun. Lett.*, vol. 13, no. 12, pp. 3479–3483, 2024.
- [12] K. Chen, C. Qi, and O. A. Dobre, "DBRAA: Sub-6 GHz and millimeter wave dual-band reconfigurable antenna array for ISAC," *IEEE Trans. Commun., early access*, 2025.
- [13] F. Rostami G., K.-K. Wong, W. K. New, H. Xu, R. Murch, and Y. Zhang, "On performance of RIS-aided fluid antenna systems," *IEEE Wirel. Commun. Lett.*, vol. 13, no. 8, pp. 2175–2179, 2024.
- [14] Z. Dong, Z. Zhou, Z. Xiao, C. Zhang, X. Li, H. Min, Y. Zeng, S. Jin, and R. Zhang, "Movable antenna for wireless communications: Prototyping and experimental results," 2024.
- [15] E. Motovilova and S. Y. Huang, "A review on reconfigurable liquid dielectric antennas," *Materials*, vol. 13, no. 8, 2020. [Online]. Available: <https://www.mdpi.com/1996-1944/13/8/1863>
- [16] Y. Shen, B. Tang, S. Gao, K.-F. Tong, H. Wong, K.-K. Wong, and Y. Zhang, "Design and implementation of mmwave surface wave enabled fluid antennas and experimental results for fluid antenna multiple access," 2024. [Online]. Available: <https://arxiv.org/abs/2405.09663>
- [17] R. Malinowski, I. P. Parkin, and G. Volpe, "Advances towards programmable droplet transport on solid surfaces and its applications," *Chem. Soc. Rev.*, vol. 49, pp. 7879–7892, 2020. [Online]. Available: <http://dx.doi.org/10.1039/D0CS00268B>
- [18] K.-K. Wong, D. Morales-Jimenez, K.-F. Tong, and C.-B. Chae, "Slow fluid antenna multiple access," *IEEE Transactions on Communications*, vol. 71, no. 5, pp. 2831–2846, 2023.
- [19] B. Liu, K.-F. Tong, K.-K. Wong, C.-B. Chae, and H. Wong, "Programmable meta-fluid antenna for spatial multiplexing in fast fluctuating radio channels," *Optics Express*, vol. 33, no. 13, p. 28898 – 28915, 2025.
- [20] J. Zhang, J. Rao, Z. Li, Z. Ming, C.-Y. Chiu, K.-K. Wong, K.-F. Tong, and R. Murch, "A novel pixel-based reconfigurable antenna applied in fluid antenna systems with high switching speed," *IEEE Open Journal of Antennas and Propagation*, vol. 6, no. 1, pp. 212–228, 2025.
- [21] H. Guo, J. Zhang, J. Rao, R. Murch, and V. K. N. Lau, "Channel estimation and analog precoding for pixel-based fluid-antenna-assisted multiuser mimo-ofdm systems," 2025. [Online]. Available: <https://arxiv.org/abs/2509.09373>
- [22] K. Chen, C. Qi, Y. Hong, and C. Yuen, "REMAA: Reconfigurable pixel antenna-based electronic movable-antenna arrays for multiuser communications," *IEEE Trans. Commun., early access*, 2025.
- [23] P. Lotfi, S. Soltani, and R. D. Murch, "Printed endfire beam-steerable pixel antenna," *IEEE Transactions on Antennas and Propagation*, vol. 65, no. 8, pp. 3913–3923, 2017.
- [24] F. Lin, "Compact design of planar quadrature coupler with improved phase responses and wide tunable coupling ratios," *IEEE Transactions on Microwave Theory and Techniques*, vol. 66, no. 3, pp. 1263–1272, 2018.
- [25] L. Guo, H. Zhu, and A. Abbosh, "Phase reconfigurable microwave power divider," *IEEE Transactions on Circuits and Systems II: Express Briefs*, vol. 66, no. 1, pp. 21–25, 2019.
- [26] Z. Wei, X. Zhu, P.-L. Chi, R. Xu, and T. Yang, "A fully reconfigurable 1x4 filtering beamforming network with continuous phase and amplitude control," *IEEE Transactions on Microwave Theory and Techniques*, vol. 72, no. 1, pp. 348–362, 2024.
- [27] B. W. Xu, S. Y. Zheng, Y. X. Li, and W. Hong, "Simultaneous amplitude- and phase-tunable power divider with wide tunable ranges," *IEEE Transactions on Microwave Theory and Techniques*, vol. 72, no. 8, pp. 4744–4756, 2024.
- [28] J. Rao, Y. Zhang, S. Tang, Z. Li, S. Shen, C.-Y. Chiu, and R. Murch, "A novel reconfigurable intelligent surface for wide-angle passive beamforming," *IEEE Transactions on Microwave Theory and Techniques*, vol. 70, no. 12, pp. 5427–5439, 2022.
- [29] W. Zheng, Y. Yang, and H. Li, "Design of polarization-reconfigurable pixel antennas with optimized pin-diode implementation," *IEEE Transactions on Antennas and Propagation*, vol. 73, no. 2, pp. 851–862, 2025.
- [30] S. Tang, Y. Zhang, Z. Han, C.-Y. Chiu, and R. Murch, "A pattern-reconfigurable antenna for single-RF 5G millimeter-wave communica-

- tions," *IEEE Antennas and Wireless Propagation Letters*, vol. 20, no. 12, pp. 2344–2348, 2021.
- [31] J. Rao, Z. Ming, J. Zhang, C.-Y. Chiu, and R. Murch, "Cost-effective enhancement of rf switch performance utilizing novel coupling structures," *IEEE Transactions on Microwave Theory and Techniques*, pp. 1–17, 2025.
- [32] R. Vaughan and J. Andersen, "Antenna diversity in mobile communications," *IEEE Transactions on Vehicular Technology*, vol. 36, no. 4, pp. 149–172, 1987.
- [33] R. E. Collin and F. J. Zucker, *Antenna theory, Part 1*. Antenna theory, 1969.
- [34] M. Khammassi, A. Kammoun, and M.-S. Alouini, "A new analytical approximation of the fluid antenna system channel," *IEEE Transactions on Wireless Communications*, vol. 22, no. 12, pp. 8843–8858, 2023.
- [35] Z. Han, S. Shen, Y. Zhang, C.-Y. Chiu, and R. Murch, "A pattern correlation decomposition method for analysis of ESPAR in single-RF MIMO systems," *IEEE Transactions on Wireless Communications*, vol. 21, no. 7, pp. 4654–4668, 2022.
- [36] K. Kreutz-Delgado, "The complex gradient operator and the cr-calculus," 2009. [Online]. Available: <https://arxiv.org/abs/0906.4835>
- [37] W. Wirtinger, "Zur formalen theorie der funktionen von mehr komplexen veränderlichen," *Mathematische Annalen*, vol. 97, no. 1, pp. 357–375, Dec 1927. [Online]. Available: <https://doi.org/10.1007/BF01447872>
- [38] S. Tang, Y. Zhang, J. Rao, Z. Han, C.-Y. Chiu, and R. Murch, "Beam-forming network design utilizing node microstrip architectures for dual-polarized endfire millimeter-wave antenna arrays," *IEEE Transactions on Antennas and Propagation*, vol. 71, no. 6, pp. 4862–4873, 2023.
- [39] "coilcraft.com," <https://www.coilcraft.com/getmedia/b3553702-9a56-/4386-b513-fcddf8709240/0402dc.pdf>, [Accessed 29-05-2024].
- [40] "murata.com," <https://search.murata.co.jp/Ceramy/image/img/A01X/G101/ENG/GJM1555C1H130GB01-01A.pdf>, [Accessed 29-05-2024].
- [41] S. Song and R. D. Murch, "An efficient approach for optimizing frequency reconfigurable pixel antennas using genetic algorithms," *IEEE Transactions on Antennas and Propagation*, vol. 62, no. 2, pp. 609–620, 2014.
- [42] J. Rao, Z. Ming, J. Zhang, Z. Li, C.-Y. Chiu, and R. Murch, "A compact shared-aperture antenna with 2-transmit and 2-receive highly-isolated ports for full-duplex MIMO systems," *IEEE Open Journal of Antennas and Propagation*, vol. 6, no. 2, pp. 422–432, 2025.
- [43] F. Jiang, Z. Zhang, M. Li, S. Shen, C.-Y. Chiu, Y. Zhang, Q. S. Cheng, and R. Murch, "Multiport pixel antenna optimization using characteristic mode analysis and sequential feeding port search," *IEEE Transactions on Antennas and Propagation*, vol. 70, no. 10, pp. 9160–9174, 2022.
- [44] J.-F. Lin, H. Deng, and L. Zhu, "Design of low-profile compact MIMO antenna on a single radiating patch using simple and systematic characteristic modes method," *IEEE Transactions on Antennas and Propagation*, vol. 70, no. 3, pp. 1612–1622, 2022.
- [45] M. Hu and Y. Li, "Wideband back cover microstrip antenna with multiple shorting vias for mobile 5G MIMO applications," *IEEE Transactions on Antennas and Propagation*, vol. 71, no. 10, pp. 8290–8295, 2023.
- [46] N.-W. Liu, B.-B. Huang, L. Zhu, and G. Fu, "Low-profile four-port patch antenna with wide isolation bandwidth and same polarization: Principle and design approach," *IEEE Antennas and Wireless Propagation Letters*, vol. 22, no. 10, pp. 2407–2411, 2023.
- [47] C. Y. Chiu, C. H. Cheng, Y. S. Wan, C. R. Rowell, and R. D. Murch, "Design of a flat fading 4 x 4 MIMO testbed for antenna characterization using a modular approach," in *2007 IEEE Wireless Communications and Networking Conference*, 2007, pp. 2913–2918.
- [48] I. J. Bahl and D. Conway, "l- and s-band compact octave bandwidth 4-bit mmic phase shifters," *IEEE Transactions on Microwave Theory and Techniques*, vol. 56, no. 2, pp. 293–299, 2008.
- [49] M. Meghdadi, M. Azizi, M. Kiani, A. Medi, and M. Atarodi, "A 6-bit cmos phase shifter for s-band," *IEEE Transactions on Microwave Theory and Techniques*, vol. 58, no. 12, pp. 3519–3526, 2010.
- [50] K.-F. Tong, B. Liu, and K.-K. Wong, "Designs and challenges in fluid antenna system hardware," *Electronics*, vol. 14, no. 7, 2025. [Online]. Available: <https://www.mdpi.com/2079-9292/14/7/1458>
- [51] J. Chen, Y. Xiao, Z. Peng, J. Zhu, X. Lei, C. Masouros, and K.-K. Wong, "Hybrid beamforming for ris-assisted multiuser fluid antenna systems," *IEEE Transactions on Wireless Communications*, pp. 1–1, 2025.
- [52] X. Lou, W. Xia, Y. Zhu, K.-K. Wong, and C.-B. Chae, "Multi-target beamforming optimization for fluid antenna-enabled multi-static isac," *IEEE Transactions on Cognitive Communications and Networking*, pp. 1–1, 2025.
- [53] H. Guo, J. Zhang, J. Rao, R. Murch, and V. K. N. Lau, "Channel estimation and analog precoding for pixel-based fluid-antenna-assisted multiuser mimo-ofdm systems," 2025. [Online]. Available: <https://arxiv.org/abs/2509.09373>
- [54] J. Robert W. Heath, J. Carlson, N. V. Deshpande, M. R. Castellanos, M. Akrouf, and C.-B. Chae, "The tri-hybrid mimo architecture," 2025. [Online]. Available: <https://arxiv.org/abs/2505.21971>